Summer 2020

Fabrication of Multifunctional Carbon Coated Cobalt Ferrite Core/ Shell Nanostructures by Pulsed Laser Ablation

Joy Roy
Missouri State University, Roy2018@live.missouristate.edu

FABRICATION OF MULTIFUNCTIONAL CARBON COATED COBALT FERRITE CORE/SHELL NANOSTRUCTURES BY PULSED LASER ABLATION

A Master's Thesis

Presented to

The Graduate College of

Missouri State University

In Partial Fulfillment

Of the Requirements for the Degree

Master of Science, Materials Science

By

Joy Roy

August 2020

FABRICATION OF MULTIFUNCTIONAL CARBON COATED COBALT FERRITE CORE/SHELL NANOSTRUCTURES BY PULSED LASER ABLATION

Physics, Astronomy and Materials Science

Missouri State University, August 2020

Master of Science

Joy Roy

ABSTRACT

Considerable research work is going on worldwide among the therapeutic scientific communities to use magnetic nanoparticles (NPs) as a controlled drug delivery system. Challenges to use those NPs for such in-vivo applications successfully are mainly biocompatibility and the functionality of those NPs. Addressing the needs, in this project, we synthesized carbon-coated cobalt ferrite (CFO) core-shell nanoparticles (CSNPS) by ablating a solution of toluene and CFO NPs with varying number of pulsed laser shots. The structure of the CSNPs then investigated through X-ray diffraction (XRD), Raman spectroscopy, and also with the high-resolution transmission electron microscopy (HRTEM). The XRD analysis shows that the inner structure of CFO remains intact after the laser ablation. The Raman data analysis confirmed that with increasing laser shots the amount of crystallinity of the carbon structure increases and the G-band peak becomes more prominent which infers fewer defects in the shell structure. The TEM images showed that the carbon is mostly present in the shell region and the intensity count from the line scan data concludes the formation of the core-shell structure of CFO NPs. Thus, the laser ablation technique turned out quite efficient to manufacture carbon-coated magnetic metal oxide CSNPs for further applications. To increase the functionality of the NPs, nitrogen was then introduced in the shell region using N, N-DMF solution along with toluene. Fluorescence spectroscopy of these two different types of coatings indicates subtle changes in the higher wavelength region, and SEM analysis informs the presence of nitrogen in the NPs although the future study is needed to confirm the existence of nitrogen in the shell structure of CFO CSNPs.

KEYWORDS: core-shell nanoparticles, biocompatibility, carbon, cobalt ferrite, ferromagneism, Raman spectroscopy, fluorescence, transmission electron microscopy

FABRICATION OF MULTIFUNCTIONAL CARBON COATED COBALT FERRITE CORE/SHELL NANOSTRUCTURES BY PULSED LASER ABLATION

By

Joy Roy

A Master's Thesis
Submitted to the Graduate College
Of Missouri State University
In Partial Fulfillment of the Requirements
For the Degree of Master of Science, Materials Science

August 2020

Approved:

Kartic C. Ghosh, Ph.D., Thesis Committee Chair

Ridwan Sakidja, Ph.D., Committee Member

Tiglet Besara, Ph.D., Committee Member

Julie Masterson, Ph.D., Dean of the Graduate College

ACKNOWLEDGEMENTS

First I would like to thank the Almighty for all the blessings I got to complete this research work successfully.

For the last two years of continuous support and guidance, I am highly grateful to my supervisor Dr. Kartik Ghosh. His motivation and ideas always directed me towards new chapters of research work. I learned the invaluable steps of methodology and characterizations under his supervision during my MS degree at Missouri State University. I would also like to thank him for his friendship, compassion, and a great sense of humor.

I would like to thank Dr. Ridwan Sakidja and Dr. Tiglet Besara for being in my thesis committee and sharing their insightful comments and helping me with propositions for future work. My sincere thanks also go to my friend Christopher Robledo and my colleague Biswajite Karmakar for helping me with data collections and analysis.

I would like to thank my parents Jyotirmoy Roy and Parul Roy for their sacrifices and blessings for which I have achieved whatever big or small in my life. I am very much thankful to Nancy Parish who has made my stay in Springfield enjoyable and nice.

My special thanks go to my beloved wife Susmita Roy for her patience, love, and all the valuable prayers for us. I dedicate this work to her name.

TABLE OF CONTENTS

LIST OF TABLES

LIST OF FIGURES

INTRODUCTION

Background

Nanostructured materials are a great tool of interest for both pure science and applied field of study. Typically ranging from 1-100 nm they have wide ranges of structural and functional properties. High surface to volume ratio of NPs plays an advantageous role for better topological property which is not available in bulk or discrete molecular structure. Their exceptional tunable physical, chemical, and biological properties have helped to build the fascinating realm of nano-biotechnology.

To save millions of lives, nano-biotechnology is at the leading edge of advancements these days in several specific fields, such as site-specific bioimaging, increasing efficiency of the drugs, targeted drug delivery, treating sophisticated chronic diseases, and so on via tailoring the unique structure and properties of NPs. The high surface to volume ratio of NPs enables researchers to enhance their optical, magnetic, and electrical properties through surface modification. As a result, with many successfully employed drug delivery systems, these NPs become useful in monitoring drug release as well.[1-4]

Nanoparticles due to their nanoscale size have the flexibility to move more freely inside our body and can be tailored at the atomic or molecular level in contrary to their bulk structures. Hence, using their unique stimuli-responsive characteristics, after attaching them to therapeutic agents, they can be used as a controlled drug release route. Along with precise localization, the other key factor that should be addressed in the case of such nanomedicines is reduced toxicity or Biocompatibility. That's why for many years large areas of scientific research have been

dedicated for controlled and biocompatible drug delivery system which can overcome the obstacles of treating complex diseases and biosensing applications.

Targeted Drug Delivery Process

Nanotechnology has changed the game of targeted drug delivery systems for the past few decades.[5] Among different mechanisms for controlled drug delivery processes have been explored, the stimuli-responsive nanocarriers have shown significant possibilities to control the release profile.[6] The design of stimuli-responsive nanocarriers in response to specific stimuli can be of two types-

1. Exogenous (variation in the magnetic field, ultrasound intensity, temperature, etc.)
2. Endogenous (variation in pH, enzyme concentration, redox gradient and so on)

Among these numerous administrative methods in the process to carry the drug to targeted regions of an organism, magnetically induced systems use permanent or alternating magnetic fields to direct the nanoparticle around the body. Without doing collateral damage this system eliminates the principal obstacle of the site-specific direction of drug delivery agents.[7] Although better control over drug delivery systems has been achieved by this system, the cytotoxicity level is one of the limiting factors of using this in nano-medicines.[8]

To overcome this factor, the coating of the magnetic core has shown promising results. Using a non-reactive coating i.e. silica, gold or silver, organic polymers, or carbon can improve the toxicity level as well as can develop the surface properties to attach therapeutic agents.[9] Carbon coated magnetic nanoparticles, in particular, are stable in strong acids and a high-temperature oxygen-free environment.[10] Therefore, in this work to achieve the desired properties coating of carbon, basically graphitic carbon coating has been done around the core structure.

Core-Shell Nanoparticles

Core-shell nanoparticle (CSNP) is a special class of nanostructure where the desired inner core, which is highly magnetic in this specific work is coated with a thin shell of benign material that protects the core against agglomeration, adsorption or chemical reaction. [11] As a result, they become oxidative stable and chemically resistant, which are attributes desired, if such materials were to be used for biomedical based applications. Moreover, this coating is enhancing its affinity to bind with drugs, receptors, ligands, etc.[3]

Ferrites as Magnetic Core

Transition metal oxides commonly referred to as ferrites, a large group of oxides that possess natural spinel-type of the crystal structure with a general chemical formula AB_2O_4 (A and B stands for octahedral and tetrahedral sites respectively). Spinel structure has a cubic unit cell with 56 atoms, 32 oxygen anions distributed in a cubic close-packed structure, and 24 cations occupying 8 of the 64 available tetrahedral sites (A sites) and 16 of the 32 available octahedral sites (B sites). With their exceptional magnetic properties, spinel ferrites can also act like a catalyst as well as sites for the growth of carbon-based shell structure which in terms of toxicity and biocompatibility making the inner core more competent.

To understand the innate magnetic properties it is important to know the crystal structure of pure CFO and associated ferromagnetism with it. CFO, in particular, has an inverse spinel structure where half of the Fe^{3+} ions occupy A sites while Co^{2+} ions and the remaining Fe^{3+} occupy B sites. Fe^{3+} ions are occupied equally, with their spin in the opposite direction, in both the tetrahedral (A) and octahedral (B) sites. Since CFO has a partially inverted spinel structure, the cobalt atoms predominantly occupy the octahedral sites. (Figure 1.1)

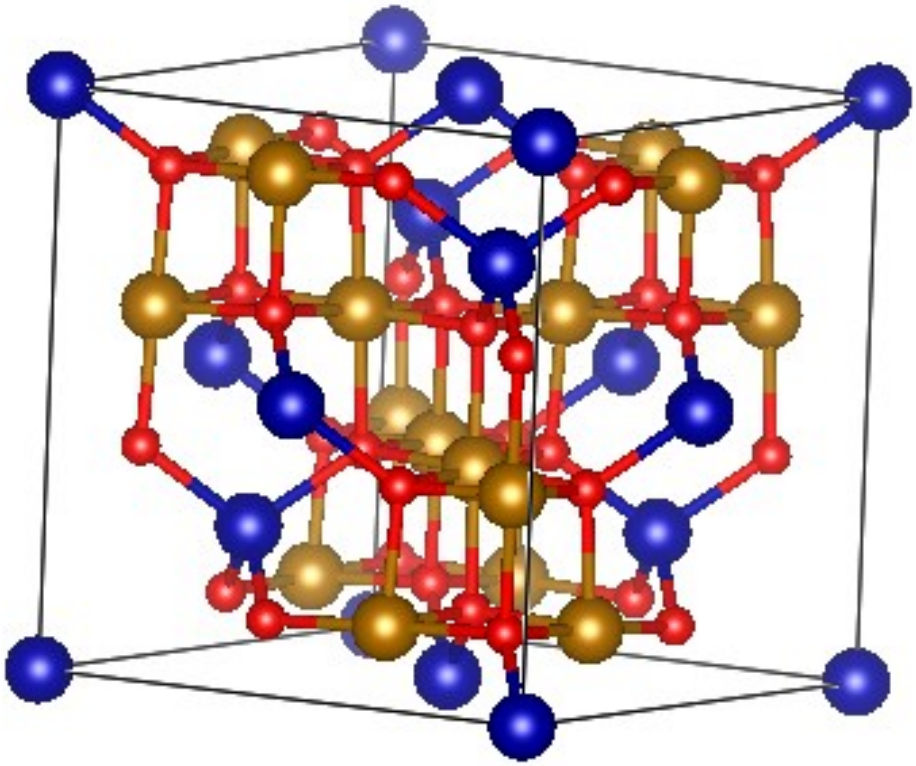

Figure 1.1: Cobalt ferrite crystal structure: oxygen ion (blue atom), cobalt ion (golden atom), and ferric ion (red atom)

The magnetic moment due to Fe^{3+} ions is zero as their spin in the opposite direction, in the tetrahedral (A) and octahedral (B) sites and thus, the net magnetic moment of the unit cell of pure CFO comes only from Co^{2+} ions with a magnetic moment of 3.87 μ_B per formula unit. This distinctive crystal structure also enables CFO to exhibit high saturation magnetization, high coercively, large magneto-crystalline anisotropy (8), and better stability among other similar candidates. These useful properties have made CFO a good candidate for the magnetic recording application. That's why recently, CFO coated with various forms of carbon structure have been synthesized for their promising biomedical application.[12]

The Functionality of the Shell

In core-shell structure, shell formation can impart novel optical, magnetic, or electronic properties in the core. So, this kind of structure can deliver multi-functionality which is most of the cases better than mono-functionality of the single-core NPs. By adding every growing shell the functionality changes according to the structure. For instance, one group shows by covering a magnetic NPs with porous silica can help to attach drugs and ensure the needed biocompatibility, while the core can concurrently be applied for targeted drug delivery to a specific organ.[13] In this work, our shell structure is made of graphitic carbon. To make activated carbon is necessary for wide use of applications as activated carbon shows much higher porosity. Chemical activation is one way to encounter this issue. Heteroatoms, such as nitrogen and sulfur can increase surface functionalities and provide control over Carbon surface chemistry.[14] Besides, by controlling the doping of nitrogen within a limiting amount the ion-storage capability and fluorescence can be improved.[15, 16] Thus, it can be said that the incorporation of nitrogen in the Carbon shell can be useful for making activated surfaces, fluorescence imaging, and drug delivery.

The present work aims at the synthesis of carbon-coated CFO CSNPs with multi-functionality. The pulsed laser ablation method has been used to synthesize the core-shell structure. Comprehensive characterization of structural and fluorescence properties of prepared NPs are conducted in this regard.

METHODS

Challenges

To make a biocompatible metal oxide magnetic nanoparticle by putting homogenous carbon coating in a solution is always challenging. The key issues involved are controlling the rate and uniformity of the coating[2] and most importantly maintaining the separation of those nanoparticles. As magnetic NPs have a natural tendency to get accumulated due to their inert magnetism. Besides, getting a sufficient level of carbon in the reaction media is essential to fabricate uniformly coated CSNPs. This work demonstrated a very clean and controlled route to cope up with those challenges.

Experimental Design

In this work, carbon coated CFO magnetic CSNPs have been synthesized by ablating the solution of CFO NPs and organic solvent. (Figure 2.1) The energy source used in this synthesis process is photon energy of a pulsed Nd: YAG laser (λ = 264 nm, repetition rate = 10 Hz, pulse

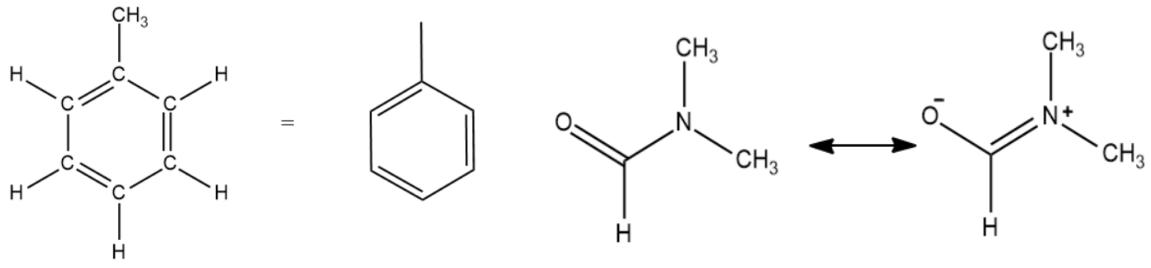

(a) (b)

Figure 2.1: Structure of the solvents: (a) Toluene, and (b) N, N-Dimethylformamide

duration = 2 ns and spot size = 3 mm) with the energy level of around 4.7 eV. To synthesize CSNPs, CFO NPs with particle size distribution from 25-30 nm, toluene ($C_6H_5CH_3$), and N, N-DMF ($(CH_3)_2NCH$) were purchased with reagent grade and used without further purification process. Toluene has a Methyl ($-CH_3$) group attached with the Benzene structure with a bond energy of 100 kcal/mole equivalent to 4.35eV. So, the energy source used is sufficient to break the alkyl group and release Carbon in the solution.[17] To incorporate nitrogen in the carbon shell and to get cyanide anions in the reaction environment avoiding the toxicity of cyanide ions, N, N- DMF, and toluene with different ratios were further used. DMF while ablating with laser can provide both carbon and nitrogen which is a unique feature of this solution.[18, 19] Figure. 2.2

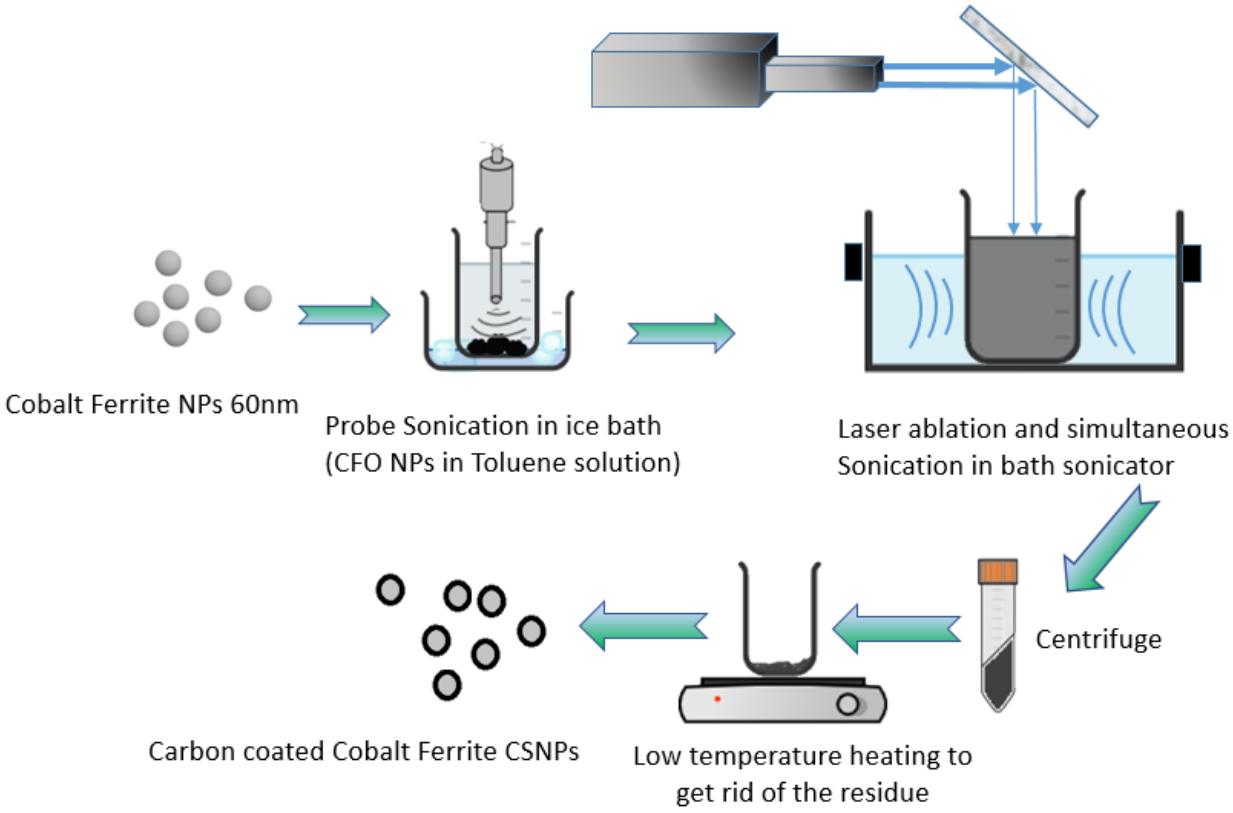

Figure 2.2: Core-shell NPs synthesis procedure

shows the overall synthesis route. As a cleaning agent, DDI water (18MΩ) was used. Every tool and beaker used during the synthesis process was washed properly using soap, DI water, Methanol, Isopropanol, Acetone, and again DI water respectively. Due to the magnetic nature of CFO NPs, two steps of sonication were performed to disperse the NPs and maintain the uniformity of the solution. Probe sonication was performed while the solution was kept in an ice bath for half an hour before the laser ablation. Probe sonication disperses and coats the NPs uniformly. After that, concurrent bath sonication and laser ablation were executed. Table 1 indicates all the sample batches synthesized in this regard.

Table 1: Experimental parameters for synthesizing CSNPs samples

Batch	Solution parameter	No. of laser shots
I	Pure CFO (10mg) + Toluene (30 ml)	5000
ii	Pure CFO (10mg) + Toluene (30 ml)	15000
iii	Pure CFO (10mg) + 25 ml of Toluene 5 ml DMF	15000
iv	Pure CFO (10mg)+ 20 ml of Toluene 10 ml DMF	15000

The extraction process involves two steps, centrifugation, and evaporation. Centrifugation for few times separates NPs from the remaining toluene solution and any residue presents in the solution. Using Methanol wash, the laser-ablated NPs were centrifuged for three times. Finally evaporating the sample in a hot plate for 20 min at 100° Celsius gave the desired CSNPs. For making carbon-coated CSNPs the above-mentioned synthesis route was followed

with only toluene solvent and for making carbon and nitrogen coated CSNPs all the synthesis steps were similar except this time N, N- DMF solvent was added along with toluene solvent. The variable in this research was the number of pulsed laser shots. This synthesis process is environmentally safe and simple. Besides, while the carbon coating is growing around CFO NPs in the solution both the NPs and carbon are staying separated from the outside atmosphere that way maintains the high purity yield of the core-shell structure.

Before producing the first batch of CSNPs, the feasibility of this project was checked by doing Infrared spectroscopy of laser-ablated and pure toluene and a field-dependent magnetic measurement of pure CFO NPs, which is the core material. After getting suitable outputs the different batches of samples were produced and various characterization tools were used to determine the properties. For structural information X-ray diffraction, Raman spectroscopy and transmission electron microscopy (TEM) were performed. For compositional analysis, SEM/EDS was done, and finally to determine the fluorescence level after nitrogen incorporation emission spectra were collected. All the basics of characterizations and results are going to be discussed in the following chapter.

RESULTS AND DISCUSSION

Infrared-Spectroscopy Analysis of Toluene

Vibrational spectroscopy is one of the fundamental tools for inspecting the structure, dynamics, and potential energy of various types of surfaces of a molecular system. The two basic types of vibrational spectroscopy are infrared spectroscopy, which depends on the absorption and transmission of IR light due to the vibration of the specific molecule, and Raman spectroscopy, which detects the light scatterings caused by the vibrations of the molecule. Depending on the different ranges of the Infrared spectrum regions, IR can be near, mid and far, one of these three types. IR absorption spectroscopy is especially the method of choice for examining the dipole-allowed vibrational modes in the molecule to identify and study different chemicals.

In this work, liquid phase toluene was used as a solvent, and the source of Carbon atoms for the shell structure. Under laser ablation, the Methyl group is supposed to break and provide Carbon ions in the solution of toluene and CFO NPs. To ensure whether toluene is breaking or not, IR spectroscopy of liquid phase toluene was performed at room temperature in Bruker Alpha II ATIR Spectrometer. The difference between as purchased and laser-ablated toluene was observed in this regard. Figure 3.1 shows the IR signals coming from particular bonds in toluene. From the interpretation of infrared (IR) absorption (or transmittance) spectroscopy, the bonds of hydrocarbon -CH (sp3), -C=C-(sp2), =C-H (sp2) are detectable. Toluene has several CH (both aromatic and aliphatic hydrocarbon) stretching absorptions in the region between 2800 and 3100 cm^{-1}.[20] When, a toluene molecule is exposed to Infrared spectrum, the benzene

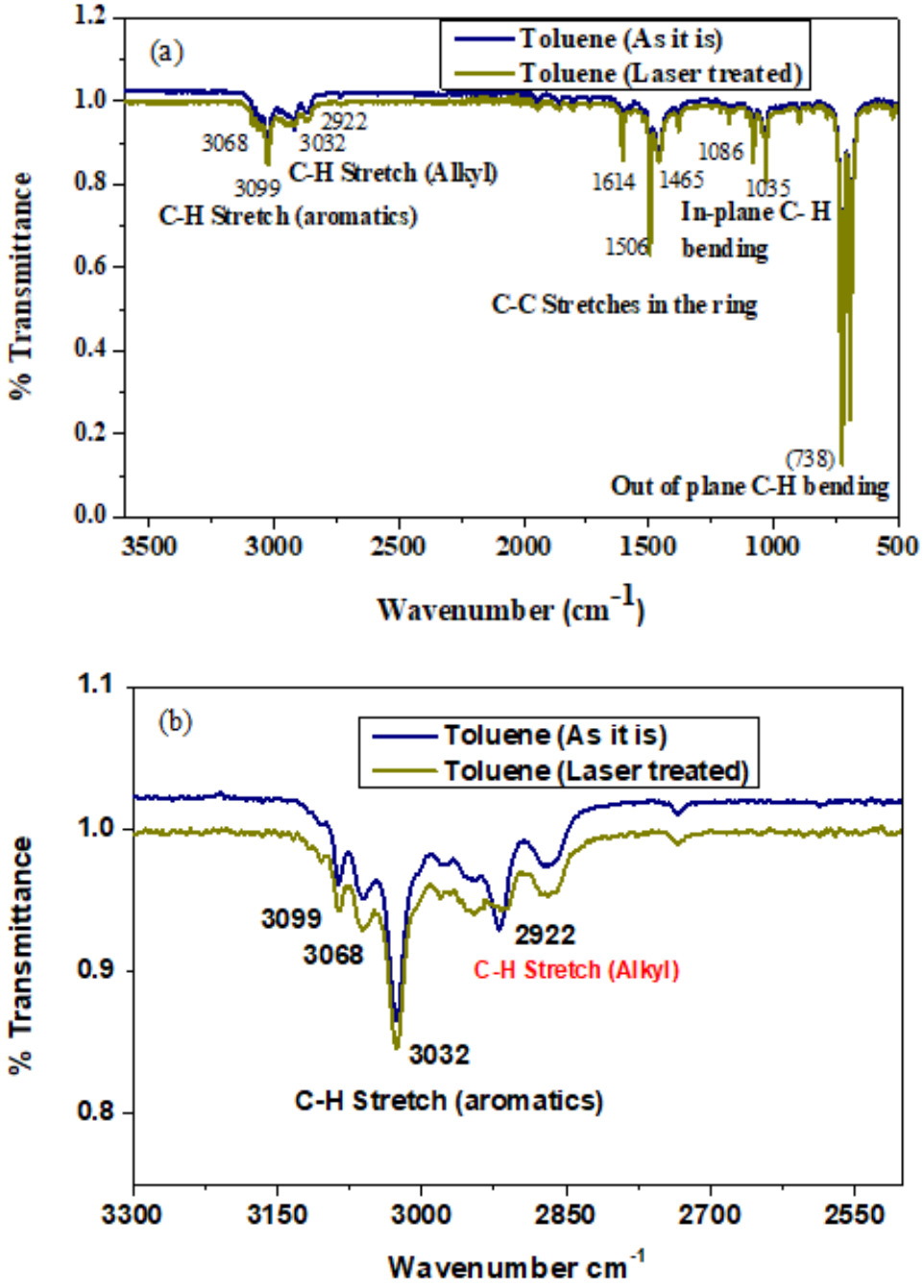

Figure 3.1: IR spectrum of liquid phase toluene: (a) Extended range showing all the IR modes of toluene (b) Narrowed range showing IR peak from Alkyl stretch of toluene

ring, (-C-C-) sp2 hybridized, alkyl group (-CH3) (sp3 hybridized) go under vibrations. As a consequence, the benzene ring stretches in the ring like a spring. In this experiment, the primary

goal is to get the carbon molecules on the surface of the core particle (CFO) by the dissociation of the alkyl (-CH_3) bond in the toluene. To obtain that alkyl bond breaking energy, a particular no of laser shots has been introduced in the liquid toluene, which has enough energy to dissociate the alkyl bond but has no impact on the sp2 hybridized benzene ring. In the lab, the laser energy was about 4.7eV which is sufficient to break the alkyl bond (100 kcal/mole equivalent to 4.35eV), however, the benzene ring has a bond strength of 113 kcal/mole which is equivalent to 4.92eV greater than the laser energy.[21] As a result, the alkyl bond dissociates from the benzene ring whereas, the aromatic benzene ring remains intact as it was. The intactness of the benzene ring can be justified by the IR spectroscopy of laser treated toluene solution. In the IR spectrum, the C-H (aromatic) absorbance (or transmittance) peak at 3032 cm^{-1} remains the same as it was before laser ablation. On the other hand, the absorbance peak at (2922 cm^{-1}) is not found, which confirms the absence of alkyl group in the laser-ablated toluene solution.

Magnetic Data Analysis of Pure CFO

The superconducting quantum interference device (SQUID) magnetometer is a very advanced experimental device to detect the magnetic flux of magnetically active samples with high precision. The relation between magnetic flux measurement and superconductivity is first introduced around 1950 when it was found that in any superconducting state the electrons of the superconductor stay in the same macroscopic level which further used by Josephson to describe Josephson junction. He showed that the changes in a magnetic field are related to a quantized flux unit. To measure the changes under a magnetic field, a constant biasing current is applied in the SQUID magnetometer, where the superconducting state is obtained by liquid helium, the corresponding voltage level oscillates with the variation in phase at the Josephson junctions,

which also rely on the fluctuation level in the magnetic flux. By computing that changes in oscillation the change in flux related to the sample can be measured. This versatile instrument has circumvented an incredible class of high-level sensing of properties related to magnetism in the field of high-temperature superconductivity, bio-magnetism, scanning squid microscope, and so on.

Magnetic field dependent magnetization data was performed using the SQUID magnetometer (MPMS-XML5, Quantum Design). Figure 3.2 shows a representative M-H plot of pure CFO NPs collected at room temperature. Observation of hysteric behavior in M-H data indicates the presence of ferromagnetism at room temperature in the pure sample. The coercive field (Hc) was around 60-70 Oe, remnant magnetization (M_R) value was 0.4 μB and saturation magnetization (Ms) was 3.87 μB. CFO has a cubic inverse spinel structure. Spinel structure has a cubic unit cell with 56 atoms, 32 oxygen anions distributed in a cubic close-packed structure, and 24 cations occupying 8 of the 64 available tetrahedral sites (A sites) and 16 of the 32 available octahedral sites (B sites). CFO has a partially inverted spinel structure with cobalt atoms predominantly in the octahedral sites. Ferromagnetism is due to cubic inverse spinel structure with oxygen anions forming an fcc closed packing and Fe^{3+} cations located at the interstitial tetrahedral sites and octahedral sites and Co^{2+} cations located at the octahedral sites. In CFO, the magnetic moment due to Fe^{3+} ions is zero as the spins of two Fe^{3+} ions are aligned antiparallel and that's why the net magnetic moment of the unit cell of pure CFO comes only from Co^{2+} ions with a magnetic moment of 3.87 μB per formula unit. In general, cation distribution can affect the structural, magnetic, and dielectric properties considerably in the inverse as well as spinel structure. For example, the substitution of rare-earth ions for Fe ion in CFO enhances the

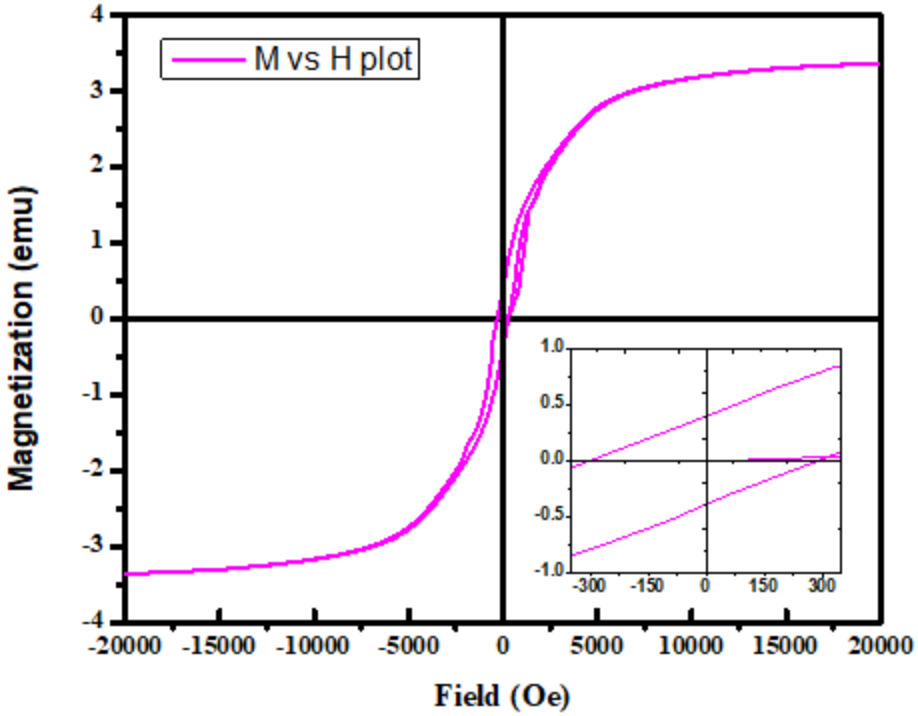

Figure 3.2: Magnetization curve of pure CFO NPs

coercive field and dielectric constant. A decrease in saturation magnetization (M_s) and Curie temperature (T_c) values were reported due to the effect of foreign atoms in CFO. There are several reports where the substitution of Mn ions in CFO results in decreasing Curie temperature as well as saturation magnetization.[22, 23]

Characterization of Carbon Coated CSNPs

XRD Analysis. X-ray diffraction (XRD) is an analytical technique for determining the atomic and molecular structure of a crystalline material, in which the crystalline structure causes a beam of incident X-rays to diffract into many specific directions. Powder XRD is used extensively for the identification of phases by measuring the diffraction angles and intensities of

these diffracted beams and comparing the resulting diffraction pattern to a reference database of diffraction data. It also provides the percentage of different phases present besides the crystal structure.

Bruker Discover D8 X-ray Diffractometer consists of a Cu K@ X-ray source with a wavelength of 1.5406 angstroms was used for the XRD analysis. For the XRD scan, the position of the detector was varied between 20^0 and 70^0 with a step size of 0.01^0. The scan speed was maintained to 6 sec/step for all the XRD data collection. The XRD patterns of pure cobalt ferrite crystal structure and core-shell structure of carbon-coated cobalt ferrite for different laser shots are shown in Figure 3.3. All the XRD measurements were done at room temperature and pressure. For structural analysis, TOPAS software was used where two standard structure CIF files of CFO and 3D Graphite were added for profile fitting.

It can be observed that the pure samples show a single CFO phase with the cubic lattice structure. The diffraction patterns identify the presence of the crystalline CFO structure. No defect or impurity phase has been detected in the XRD pattern denotes that the purchased CFO NPs are highly pure. Rietveld structure analysis using Topas software gives a crystal size of around 25 nm which is a little lower than the average crystalline size (28 nm) of the nanoparticles. CFO Miller indices of (220), (311), (222), (400), (422), (511), and (440) have been successfully identified in the pure and laser-ablated NPs. The goodness of the fit (GOF) for the CSNPs is 1.23. Increasing the number of laser shots has almost no effect on their XRD pattern. However, the phase percentage changes significantly in the Rietveld analysis reveals the presence of the second phase in the NPs. Table 2 below shows the comparison among the samples for the lattice parameter, crystallite size, and amount of phases present. With increasing shots, the lattice parameter didn't change that much but the crystallite size has changed due to

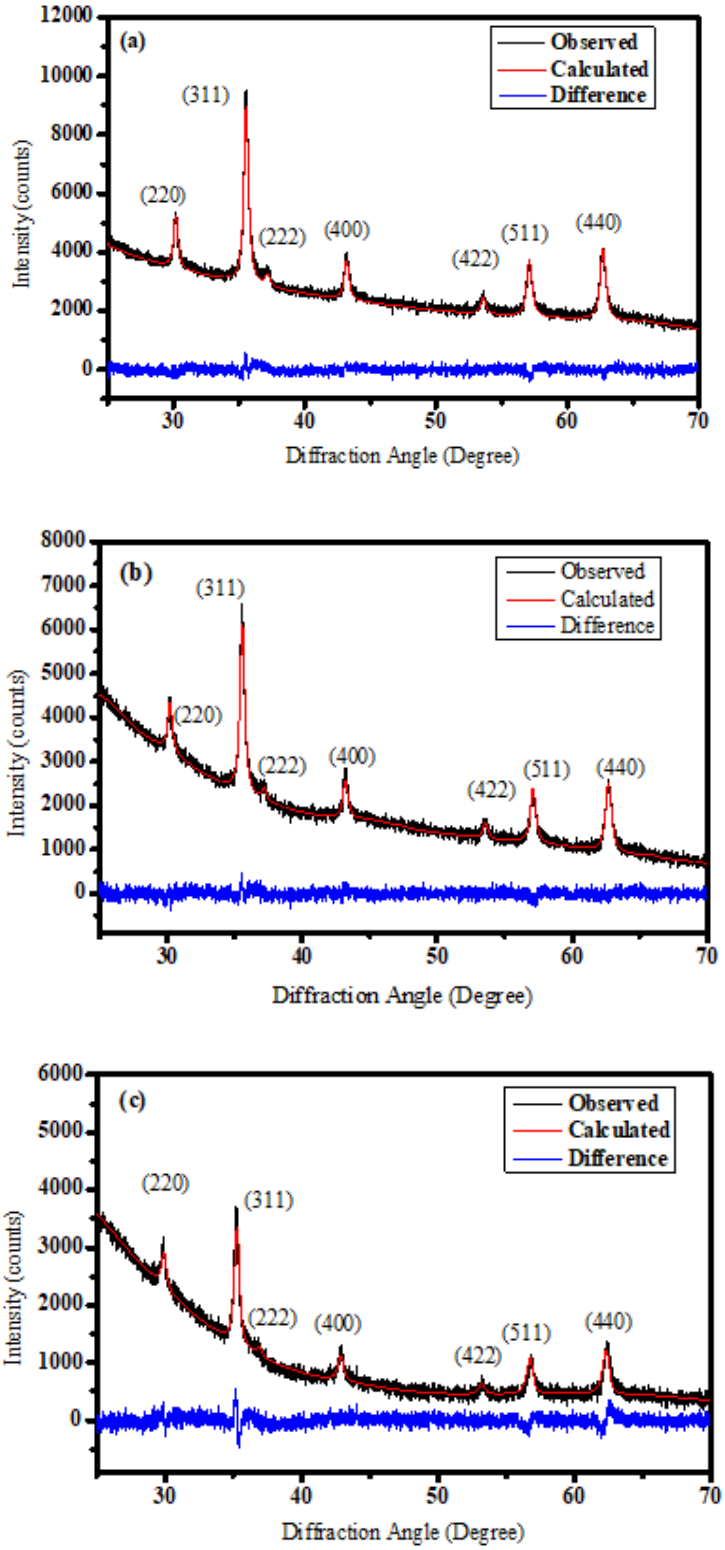

Figure 3.3: X-ray diffraction patterns for the nanoparticle samples (a) Pure CFO NPs (b) CFO NPs after 5000 laser shots (c) CFO NPs after 15000 laser shots.

Table 2: Diffraction results of pure and laser-ablated CFO NPs samples in Toluene solvent.

Batch (NPs)	Lattice parameter of CFO (Å)	Crystallite size (nm)	Phases present (percentage)	
			CFO	Graphite
Pure CFO	8.39	25.4	99.75	0.25
CFO_C (5k shots)	8.39	26.4	95.72	4.28
CFO_C (15k shots)	8.41	30.2	92.15	7.85

coating thickness. Also, with an increasing amount of carbon, the presence of dual phases becomes more prominent. That suggests the growth of carbon around the CFO core particles.

The graphitic peak count, compared to the CFO structure is actually in the noise level and so it cannot be detected. (Figure 3.4) Besides, the signal coming from the core structure and the background effect might suppress the signal diffracting from the thin shell. Therefore, XRD analysis cannot provide a comprehensive idea of carbon structure in the CSNPs.

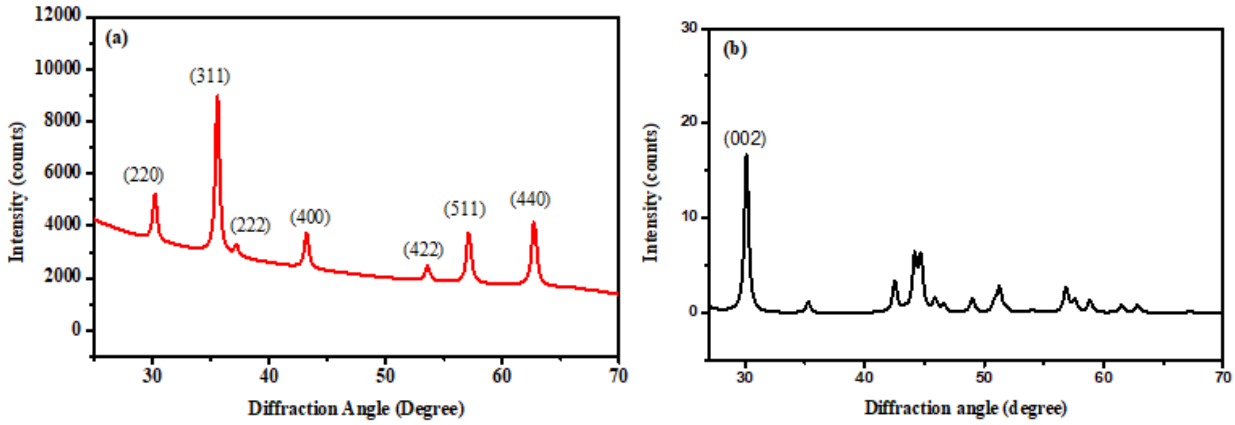

Figure 3.4: Calculated data generated from standard structure file (a) cobalt ferrite (b) graphitic carbon

Raman Spectroscopy Analysis. Raman spectroscopy can verify very subtle changes in the crystallinity, presence of impurity atoms, doping effect, and surface disorders.[24] Raman shift can efficiently detect structural and vibrational properties of different ferrites. CFO as mentioned earlier belongs to the inverse spinel-type cubic structure with the Fd3m space group. In CFO the two different types of cations can be surrounded by either six anions forming an octahedron or four anions forming a tetrahedron. CFO and ferric Oxide (Fe_3O_4) has similar space group and so the X-ray powder diffraction pattern cannot differentiate between CFO and Fe_3O_4, but their Raman spectra can determine the difference quite efficiently. One unit cell of cubic CFO symmetry contains 56 atoms and the smallest Bravais cell contains only 14 atoms. So, 42 vibrational modes are available. Among which, group theory separates the following optical phonon distribution: namely $A1_g$ (R), E_g (R), $T1_g$, $3T2_g$ (R), 2A2u, 2Eu, 4T1u (IR) and 2T2u. out of which five ($A_{1g} + E_g + 3T_{2g}$) are Raman active modes depending on the vibration of O^{2-} anions and both octahedral and tetrahedral site cations.[25]

Room temperature Raman spectra for all the powder samples in this work were done in Renishaw confocal Raman spectroscope where detailed, chemical images and highly specific data from discrete points were able to be detected. All the spectral raw data were collected using a monochromatic green laser of excitation wavelength of 532 nm. Figure 3.5 shows the background-subtracted Raman shift of pure and Laser ablated CFO NPs. The XRD plot discussed earlier showed almost similar results for both types of NPs. So, no consensus has been able to be drawn as yet. But if we look at the Raman spectra of the for the experimental data of pure and laser ablated samples without any fitting or deconvolution it is visually evident that pure NPs and laser-ablated NPs has different peak positions and peak intensity. Pure CFO

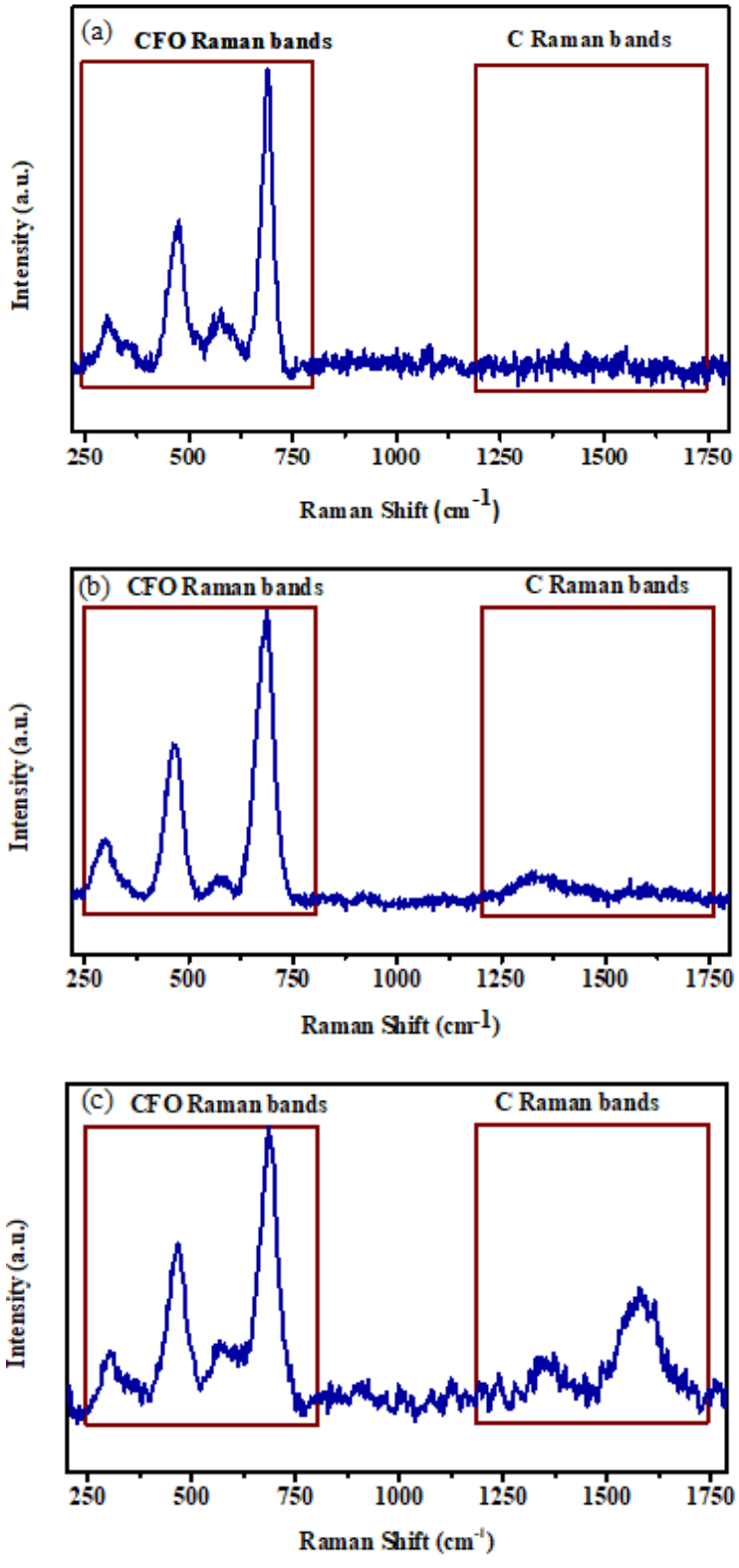

Figure 3.5: Raman spectroscopy of NPs samples (raw data) (a) Pure CFO NPs (b) CFO NPs after 5000 laser shots (c) CFO NPs after 15000 laser shots.

sample shows the characteristics Raman modes associated with the spinel structure and there is no Carbon or graphitic bands from 1200 to 1800 cm^{-1}. On the other hand, the laser-ablated CFO samples reveal graphitic bands quite clearly in the higher wavenumber. Figure 3.5 (b and c) are Raman spectra for two different no. of laser shots. After 5000 shots the presence of carbon is visible but the intensity count is very low, suggests that laser ablation is releasing carbon from the toluene solution and those carbon ions are getting bonded with the CFO NPs. But in the initial stage, most of the signals related to the graphitic structure are coming from lower wavenumber which is the monocrystalline defect structure of graphite. With increasing laser shots from 5000 to 15000, the CFO Raman modes show few changes. The one specific difference which is visually detectable is the shoulder band shape-changing around 550-600 cm^{-1} position. The most noticeable difference is the vibrational modes coming from graphitic Carbon. Besides, the peak associated with crystalline graphite in the higher wavenumber is dominant than the defect peak Figure 3.5 (c). The intensity counts reasonably displaying the fact that more and more carbons are bonding with the CFO NPs and the carbons growing around the NPs are trying to form a periodic structure when they are available in the reaction media for a longer duration.

To determine the position of the different vibrational modes and showing the precise changes related to different sites of the crystals a least-square fit with the Lorentzian line shape was used to fit the Raman spectra. The structural changes of CFO NPs with laser ablation are displayed in the frequency range of 200-800 cm^{-1}. And the formation of graphitic shell around the CFO NPs are visible from 1000-1800 cm^{-1} Raman shift range. That's why the deconvolution of the peaks are divided into these two regions and Figure 3.6 and 3.7 are generated according to this division.

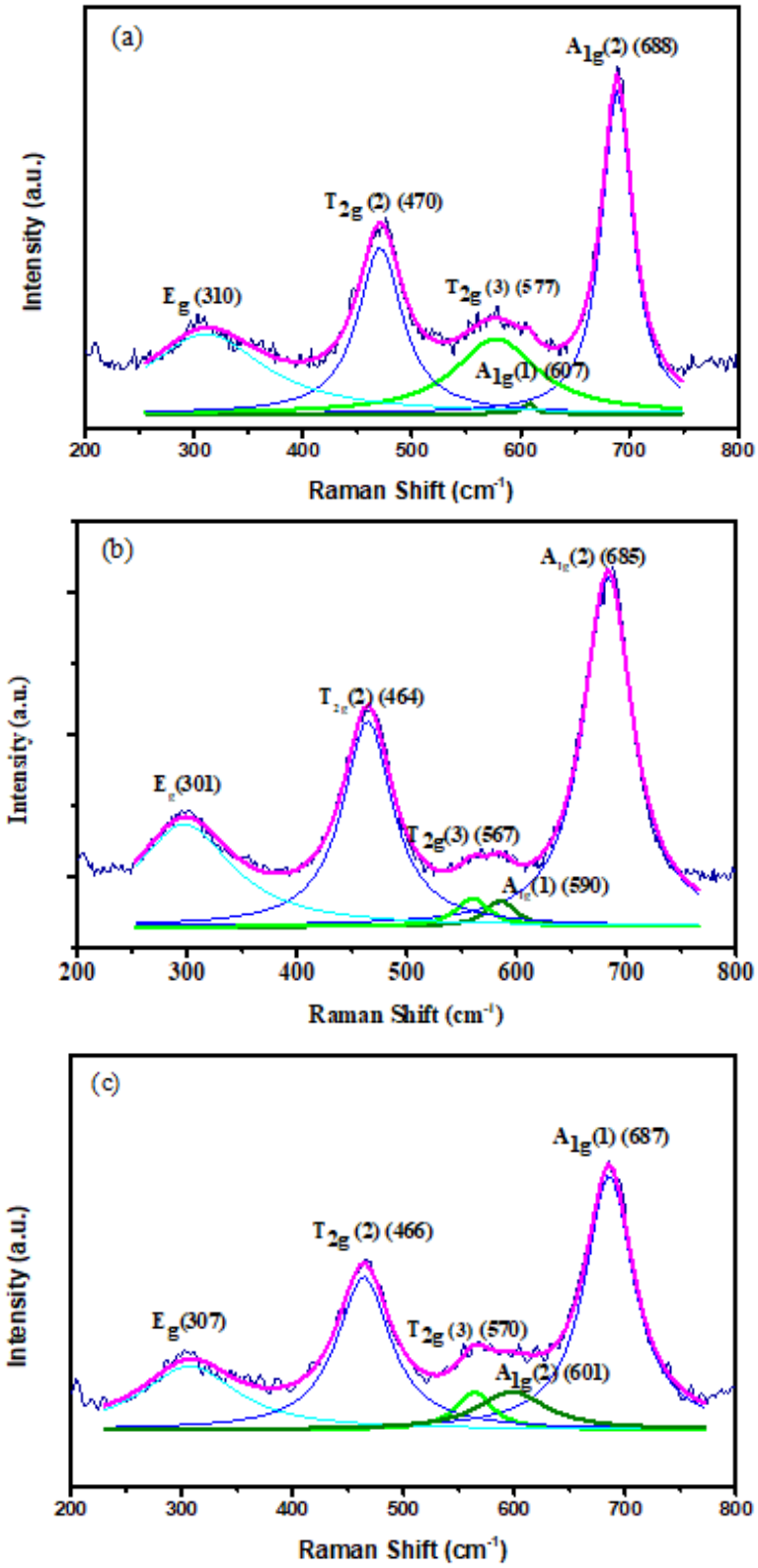

Figure 3.6: De-convoluted and fitted CFO Raman modes of NPs sample (a) Pure CFO NPs (b) CFO NPs after 5000 laser shots (c) CFO NPs after 15000 laser shots.

Pure CFO shows the broadband around 310, 470, 577, and 607 cm^{-1} and a strong band around 688 cm^{-1}. By looking at the CFO crystal structure, the octahedral sites are occupied by both Cobalt (Co^{2+}) and Iron (Fe^{3+}) ions, and the tetrahedral sites are only occupied by Fe^{3+} cations. Due to the different ionic radius, when Co^{2+} (0.58nm) and Fe^{3+} (0.485nm) cations try to bond with O^{2-} to form octahedron the cationic redistribution between the two bonds Fe-O and Co-O causes a structure similar to a doublet. The Raman shift around 610 and 690 cm^{-1} are associated with the vibration modes coming from the stretching vibration of Fe^{3+} and O^{2-} ions in the A sites. The T_{2g} (3), T_{2g} (2), and E_g around 580, 470, and 310 cm^{-1} respectively are lower wavenumber Raman modes related to the vibration in the B sites. Now, if we go from pure to laser ablated samples, we can see the counts for the A_{1g} peak is increasing with increasing laser shots. That suggests that some Carbon ions from shell layers may enter into the octahedral sites of the CFO crystal.

Figure 3.7 shows the Intensity vs Raman shift for laser ablated samples from 1000- 1800 cm^{-1} range, fitted and de-convoluted to detect the presence of Carbon and measure the amount of crystallinity in the shell structure with the increasing number of shots. The Raman signals coming from the Carbon has both amorphous and crystalline feature. There are two or three humps present in the diagram, associated with those periodic (G-band) and non-periodic (D-band) structure. The peaks in the lower wavenumber regions (1200-1450 cm^{-1}) stand for amorphous Carbon or called defect structure, whereas the higher wavenumber (1500-1600 cm^{-1}) peaks are coming from periodic graphite structure. The presence of disorder in sp2-hybridized carbon systems results in resonance Raman spectra, and thus makes Raman spectroscopy one of the most sensitive techniques to characterize disorder in sp2 carbon materials. Figure 3.7(a) is for the NPs sample after 5000 laser shots, which has both D and G-band centered at around 1350

and 1601 cm^{-1} respectively. The standard D and G-band appear at 1340 and 1583 cm^{-1} which is kind of close to the Raman shift of the sample. Besides, the peak at 1601 cm^{-1} can be splitting of G-band due to randomly distributed surface structure. The G-band usually splits into two peaks

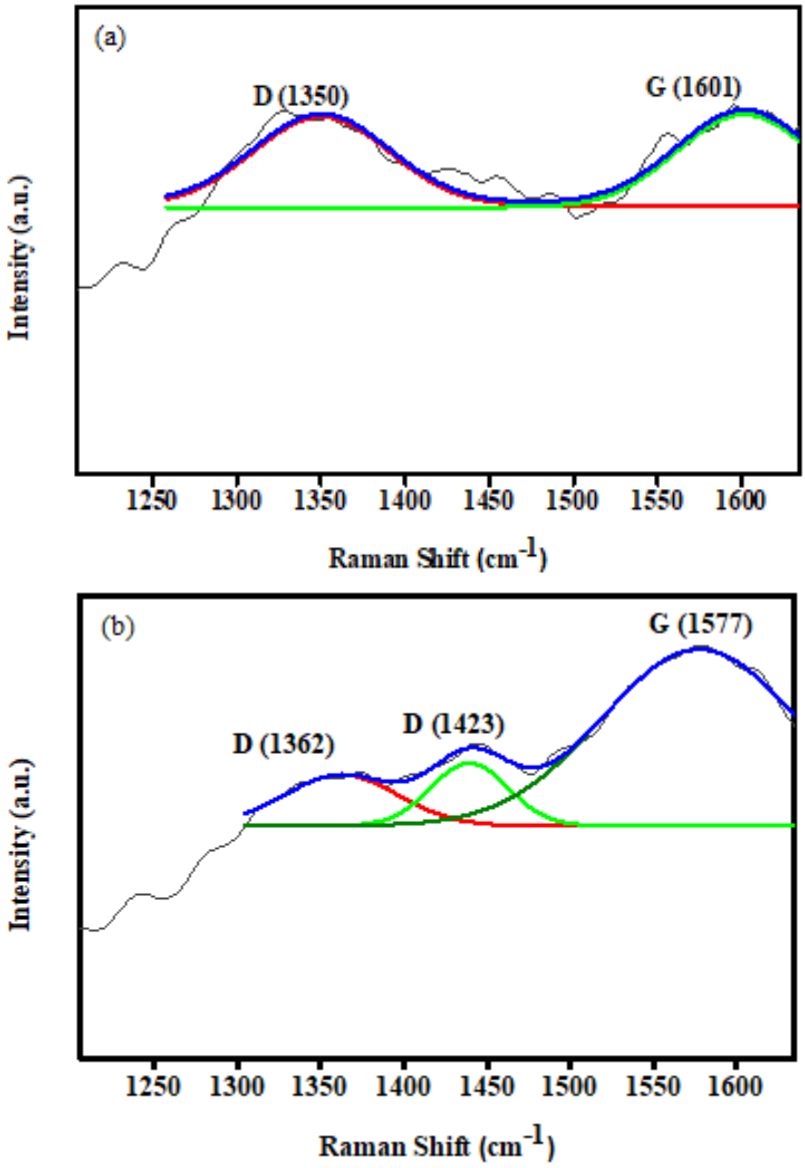

Figure 3.7: De-convoluted and fitted graphite Raman bands of NPs sample: (a) CFO NPs after 5000 laser shots (b) CFO NPs after 15000 laser shots. (Blue represents the cumulative fitted plot)

around 1580 and 1620 cm^{-1} due to the interaction of localized vibrational modes with extended phonon modes. However, in Figure 3.7(b), after 15000 laser shots the G-band position is very close to the standard wavenumber. Here, the D band breaks into two peaks 1362 and 1423 cm^{-1} due to the transformation from disordered to an ordered state.

The relative intensity count between the D-band and G-band (I_D/I_G) is the characteristic of the relative amount of ordering in the Carbon shell structure. So, the I_D/I_G ratio increases when more amount of crystallinity presents in the Carbon structure. Amorphous carbons are made of non-periodic pentagons and hexagons rings. These hexagons go down and start to appear aromatic rings of hexagons when the number of crystallinity increases. Therefore, when the I_D/I_G ratio decreases, the quantity of the groups with sp^2 hybridization goes up, developing a periodic structure known as graphitic structure.[26] In summary, an increase in the laser ablation number causes the deposition of additional carbon onto the core. Besides, a decrease in defects of the deposited layer can occur.

The Raman spectroscopy has shown outstanding results on the changes in the structure and formation of CSNPs in this work. From this analysis, it is evident that graphitic 3D carbon layers are growing around the CFO core structure. Also, there is no free carbon, instead, the carbons in the reaction media are making bonds with CFO NPs. Due to this bonding, some structural changes are occurring in the CFO crystal structure which has been observed in the CFO Raman bands. Thus, Raman analysis helps to see very subtle to noticeable changes that happen during the formation of CSNPs structure. In the next discussion on transmission electron microscopic (TEM) analysis the correlation of the spectral analysis from Raman data will be established.

TEM Data Analysis. Transmission Electron Microscope (TEM) provides structural and chemical information with a very high spatial resolution. Quantitative chemical analysis in areas smaller than 1 nm can be done using TEM. While light microscopes work in the visible wavelength (400-700 nm) range, Electron microscopes use electron beams, which is ten thousand times shorter than the visible light and allows resolution down to 0.1 nm. This electron beam of very high energy is produced from a metal filament under a high vacuum and then converged onto the sample using a magnetic lens. Cryogenic stages are used to reduce the electron beam induced heating and contamination. In scanning transmission electron microscope (STEM) the electron beam is focused as a fine probe on the sample and rastered across the sample to record the transmitted intensity using a high angle annular dark field (HADDF) detector.

Using the concept of the strong interaction between an electron and solid, the variation of intensity of the TEM image is achieved. To generate a TEM image of a specimen, it has to be very thin. The electrons are scattered from the sample elastically or in-elastically while penetrating the sample. That's why the specimen thickness has to be very small (>100nm) to mitigate the broadening of the electron beam. As electrons are wavelike, some of them are diffracted (elastic interaction) and some of them are transmitted without losing any energy from the sample. Both of these electrons produce the signals for the detector to catch and generate crystallographic information. Another feature associated with TEM is the energy dispersive spectroscopy known as TEM- EDX. Electrons bombarding onto the sample also cause it to emit X-rays due to inelastic scattering whose energy is characteristic of the elemental composition of the sample. X-ray microanalysis uses an energy dispersive X-ray (EDX) spectrometer to count and sort characteristic X-rays according to their energy.

For the TEM data collection of the CSNPs, a small drop of CSNPs in ethanol solution was cast onto thin lacey Carbon support on a Cu TEM grid and then dried in air. High-resolution TEM (HRTEM) images were formed at ambient temperature using 200 kV energy and aberration-corrected Titan 60-300 high coherence, high brightness, field emission electron gun (FEG) which is equipped with a Cs- image corrector and an electron gun monochromator to provide useable probe current with an energy resolution of 0.15 eV. This TEM particularly optimized for the investigation of soft and bio-materials with both high-resolution imaging and the ultimate in chemical analysis capabilities. The images are rendered with 500*550 pixels by a charge-coupled device camera (CCD). Energy-dispersive X-ray spectroscopy (EDXS) was performed at 200 kV using a Tecnai F20 with an X-TWIN objective lens and high brightness FEG. The objective lens design allows for efficient collection of X-rays for elemental analysis down to the sub-nanometer level.

Figure 3.8 shows the colored TEM images for different elemental mapping which explains the overall topography and distribution of the atoms in the core and at the surface of the CSNPs. The very first valuable information TEM image shows here that, the NPs are well dispersed in the grid. From the TEM image Figure 3.8 (a, b, c, d, e, and f), it is visible that the Co, Fe, and O are present uniformly in the NPs sample and show high contrast as they form the core of carbon-coated CFO CSNPs. The faded image (Figure e) of carbon mapping confirms the presence of carbon in the structure. Although the lacey carbon grid was used for the support the contrast of the image visually indicates that carbon is following the NPs everywhere they are being attached with the grid or outside the grid. Besides, an increase in the Carbon atom count in the surface/ interfaces confirms the shell structure of graphitic Carbon.

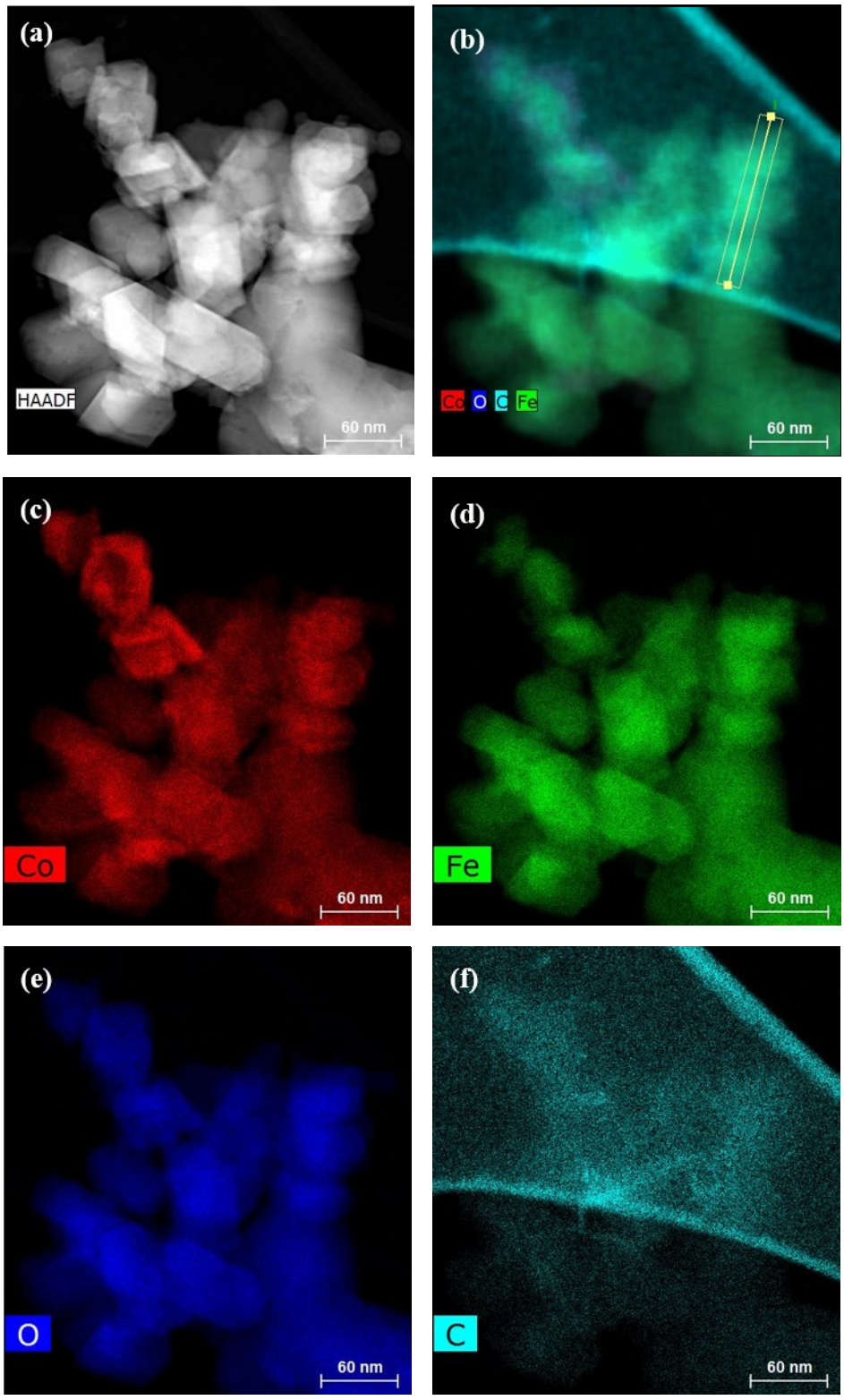

Figure 3.8: TEM colored mapping of the CSNPs: (a) sample region for HAADF imaging, (b) mapping of the CSNPs, (b) intensity from the Co atom, (c) intensity from the Fe atom, and (d) intensity from the O and (e) intensity from C atom.

Observed line scan of the CSNPs, which is shown in Figure 3.9, additionally supports the core-shell nature present in the material. The yellow straight line in Figure 3.9a illustrates the scanned region for the quantitative analysis presented. in Figure 3.9b. Line scan through the interface provides conclusive evidence of the incremental Carbon count in the interface. This line-scan also illustrates that shell atom in the core region is the lowest among all the atoms. A

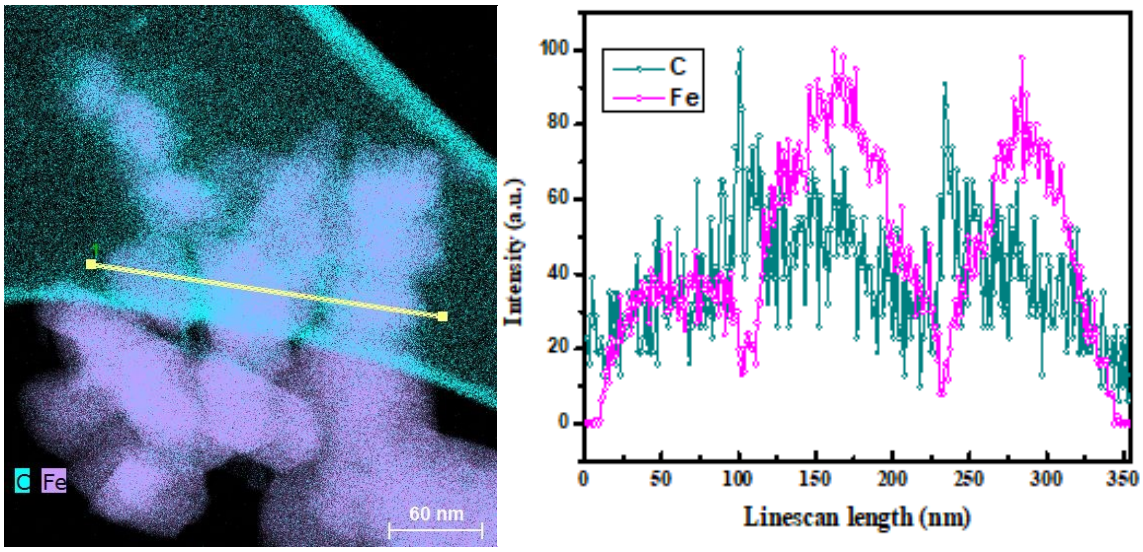

Figure 3.9: (a) TEM-EDX showing Fe, C intensity at the region of interest for the quantitative analysis (yellow line). (b) Intensity along the yellow line.

slightly higher count for the Carbon in the two most outside points of that yellow line indicates the possibility of Carbon signal coming from the lacey Carbon, not the NPs. Other than the interface region, the count of Fe atom increases significantly in the core region which is an expected outcome due to the formation of the core-shell nanostructure. The size of the average core diameter is 35 nm and shell diameter distribution thickness varies between 1 to 3 nm.

Characterization of CSNPs after Nitrogen Incorporation

The CFO@C CSNPs structural and elemental analysis have shown favorable results for using them as a medium for controlled drug delivery. Though cyto-toxicity measurement is a prior criterion to explore the biomedical applications, the formation of periodic carbon shell around the NPs should decrease the toxicity level and solve the limitation of biocompatibility of the NPs. As we have discussed earlier that, for drug delivery using magnetic CSNPs the functionality of the shell material also plays a vital role in choosing that magnetic NPs. Nitrogen addition in the shell means there will be some form of bonding between carbon and nitrogen which has undoubtedly better-attaching capability than graphitic carbon as then the carbon shell will be more activated than before. The two samples (batch III and IV) for varying the ratio of toluene and DMF (5:1 and 2:1) and constant laser shots, our goal was to introduce nitrogen in the shell material. X-ray diffraction, Raman and fluorescence data analysis were performed to determine the changes in structure and fluorescence of the CSNPs.

XRD Analysis. Figure 3.10 shows the X-ray diffraction pattern of CFO_C and synthesized CFO_CN (1) and CFO_CN (2) samples. The spectroscopy peaks located over the diffraction angle 20–70^0 associated with the miller indices of (220), (311), (222), (400), (422), (511) and (440) planes. They belong to the cubic spinel structure. The position of the diffraction peak remains similar after the laser treatment in toluene and DMF solution as it matches after fitting them with the standard CFO structure. Lattice parameter and crystallite size were calculated by refining the structure using Topas software. The Rietveld refinement infers the presence of dual-phase after the laser ablation. Table 3 shows the comparison of all the laser-treated samples under different reaction medium. As there is no shift in diffraction peaks, it suggests that there was no substitution of metal ions. The increase in lattice parameter may

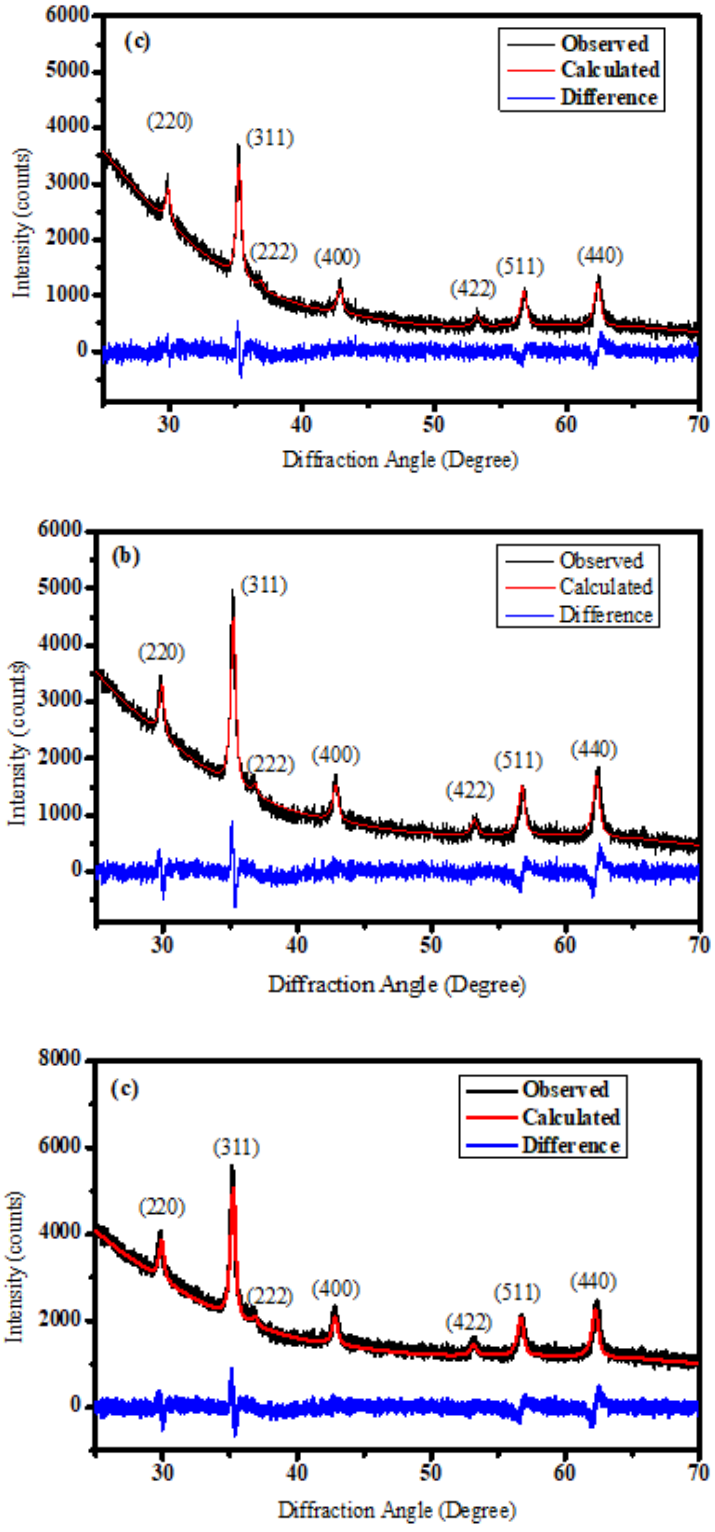

Figure 3.10: X-ray diffraction patterns for the nanoparticle samples after 15000 laser shots: (a) CFO_C (Batch II) (b) CFO_CN (1) (Batch III) and (c) CFO_CN (2) (Batch IV)

occurred due to the preferential occupation of A and B sites by carbon atoms. Not much shrinking of the peaks is visible though average crystallite size changes. If we compare

Table 3: Diffraction results of CSNPs before and after N, N- DMF addition

Sample Batch (NPs)	Lattice parameter of CFO (Å)	Crystallite size (nm)	Phases present (percentage)	
			CFO	Graphite
CFO_C (15k shots)	8.41	30.2	92.15	7.85
CFO_CN (1) (15k shots)	8.41	27.4	96.2	3.8
CFO_CN (2) (15k shots)	8.40	30.2	98.1	1.9

this data table with table 2 of carbon-coated CFO structures, we can see the phase percentage of graphitic phase decreases with the addition of DMF solution. Also for higher ratios of DMF compared to toluene, decreasing the phase percentage of crystalline graphite even more. The presence of DMF in the reaction media provides both carbon and nitrogen as we have discussed earlier. So, instead of just forming graphitic structure now carbon has more options and thus resulting in different functional groups. Other than graphite and CFO there might be another phase present in the structure. But until now, which functional group is forming is not confirmed and as there are so many organic structures possible with carbon and nitrogen it's quite difficult to choose a standard structure file besides CFO and graphitic carbon.

Raman Spectroscopy Analysis. The Raman spectra for CFO_CN (2), which has been synthesized with a higher amount of DMF was performed in Horiba Jobin Yvon LabRAM, model- HR800 Raman spectroscopy machine. The excitation wavelength was similar to before, 532 nm green laser. From Figure 3.11 the characteristics of vibrational bands associated with

CFO inverse spinel structure are observed in both pure CFO and CFO_CN (2) samples located in the range of 200-800 cm^{-1} range. The interesting feature of the CFO_CN (2) Raman spectra shown in Figure 3.11(b), is the photoluminescence, that is highly visible in the higher wavenumber region. This photoluminescence has made it difficult to detect the graphitic bands available in the 1200-1700 cm^{-1} wavenumber region.

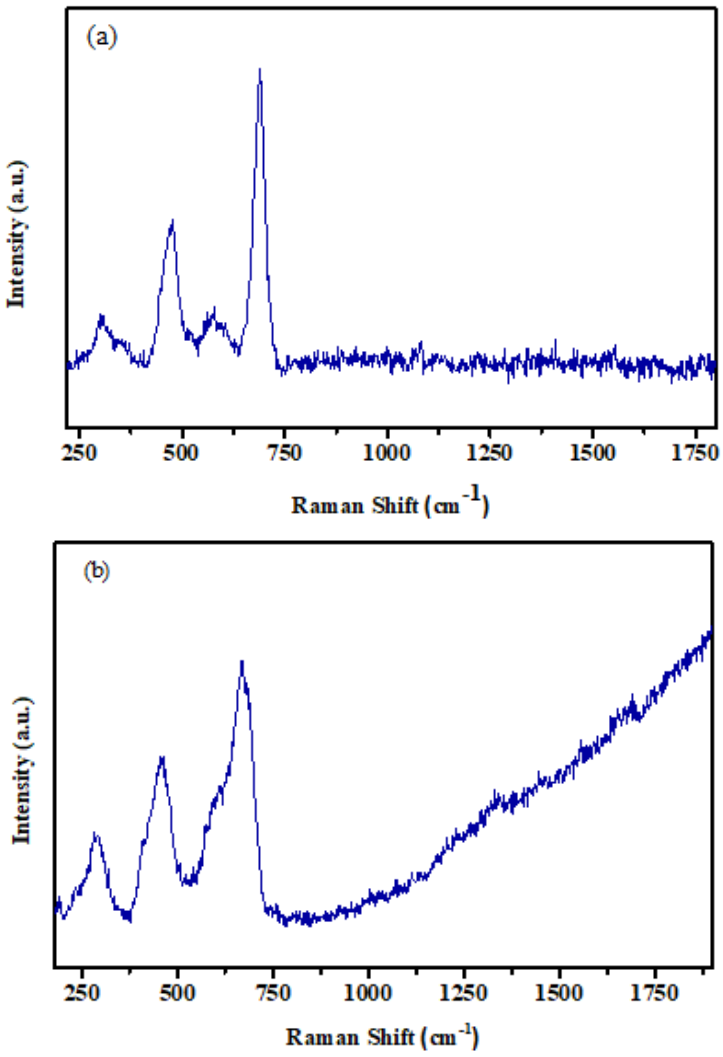

Figure 3.11: Raman spectroscopy of NPs samples (raw data): (a) Pure CFO (b) CFO_CN (2) (Batch IV)

For fitting the peaks a least-square fit with Lorentzian function was used. Figure 3.12 shows the deconvoluted peak positions for different Raman active peaks of CFO crystal structure. As the Raman spectrum for the pure CFO sample was discussed earlier here we will just compare the differences between pure CFO and treated CFO_CN (2) samples. The broadbands are located at 288, 454, 573, and 600 cm^{-1} and a strong band around 678

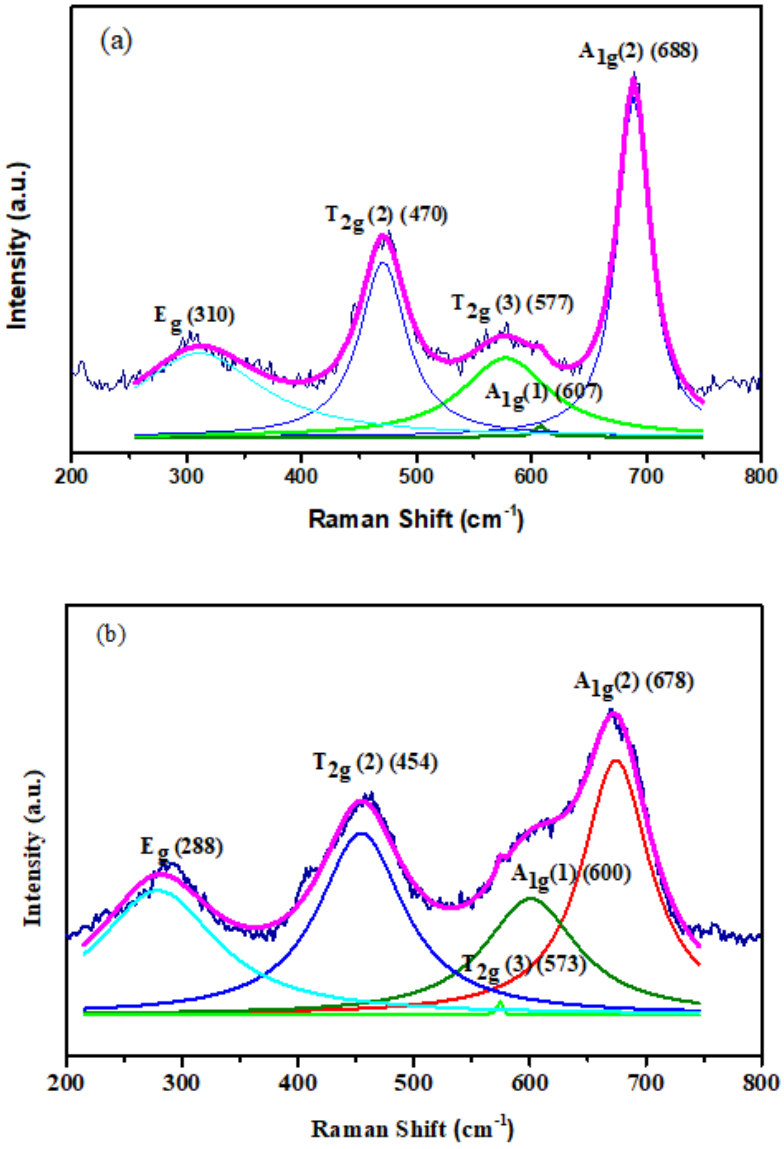

Figure 3.12: De-convoluted and fitted CFO Raman modes of NPs sample: (a) Pure CFO NPs (b) CFO_CN (2) NPs (Batch IV)

cm^{-1}. The position of all the peaks compared to the pure CFO has shifted towards lower wavenumber. This red shifting might be related to the higher molar mass of the NPs as a very small amount of carbon or nitrogen may have entered into the octahedral or tetrahedral voids. Another feature observed in Raman modes of these two diagrams is that the peak intensity and line width of A_{1g} (2) and T_{2g}(3) changed with the DMF addition and laser shots. The shoulder peak A_{1g} (2) is attributed to the stretching of Fe^{2+} ions and O^{-2} ions in the octahedral sites. This surely tells that few numbers of carbon or nitrogen may have traveled to the A sites and increased the vibration level. Both of these two atoms are lighter and the atomic radius of carbon and nitrogen is 70 and 65 pm respectively which truly suggests their migration towards void sites. Other bands count remains more or less similar except E_g which is associated with the vibration of tetrahedral voids. If we compare Figure 3.6c and Figure 3.12c, indeed we can see there is a change in the intensity count. As tetrahedral voids are smaller in size than octahedral voids, the nitrogen atom has a higher probability to enter into that sites than carbon atoms. This might have changed the vibration level in the A sites of the CFO_CN (2) sample. Finally, as due to photoluminescence no carbon bands were visible in the spectrum. So, to get the information regarding carbon structure another characterization tool has to be employed.

Fluorescence Data Analysis. Fluorescence is a kind of luminescence caused due to exciting a molecule by photons, resulting in shifting of its electrons towards a higher excited state. This causes the singlet ground state promoted to a singlet-excited state. Finally, as the excited electrons return to the ground state, emits a photon of lower energy, which corresponds to a longer wavelength, than the absorbed photon. Thus emission spectrum is generated which is called Fluorescence spectroscopy.

To understand how the presence of nitrogen tunes the shell structure and functionalities concerning photon energy absorption, the fluorescence spectra were taken. Figure 3.13 below shows standard emission spectra for DI water and DI water and CFO solution, measured to calibrate the instrument. The corresponding emission peak of DI water for 350 nm excitation wavelength is around 395 nm which is the same in this Figure below.

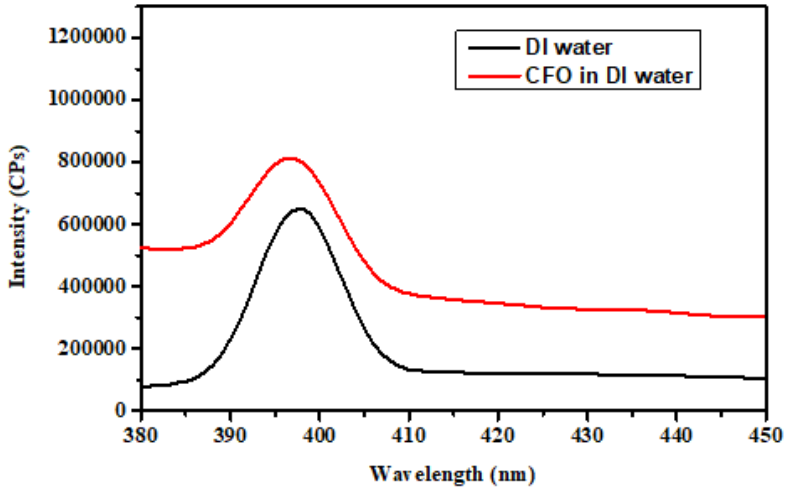

Figure 3.13: Emission peak of DI and DI water nixed with CFO NPs

After calibrating the instrument, first, the Raman for 3D carbon structure was measured as it was not possible to detect in the actual Raman spectrum. From the energy difference between the incident and scattered vibrational levels, ν, the Raman shift in wavenumbers (cm^{-1}), is calculated. Using this concept, for different excitation energy first the emission spectra were measured. Then the Raman shift was calculated for individual excitation wavelength and corresponding emission wavelength. Figure 3.14 below shows the calculated Raman spectrum for CFO_CN (1) and CFO_CN (2) samples. The G-band peak is visible around the 1450-1600 cm^{-1} wavelength region. With a change in excitation wavelength towards higher value, the

Raman peak has shifted towards left which is not expected. So, to check the calibration again, the Raman shift of DI water for different excitation energy was calculated. (Figure 3.15) Since the position of 3300 cm^{-1} characteristic peaks for DI water is shifting too, the calibration considering DI water has to be done every time for different excitation wavelengths. Another thing is that all the peaks are broadened. The reason is, the fluorescence instrument excites with a range of ±10 nm from the selected excitation value.

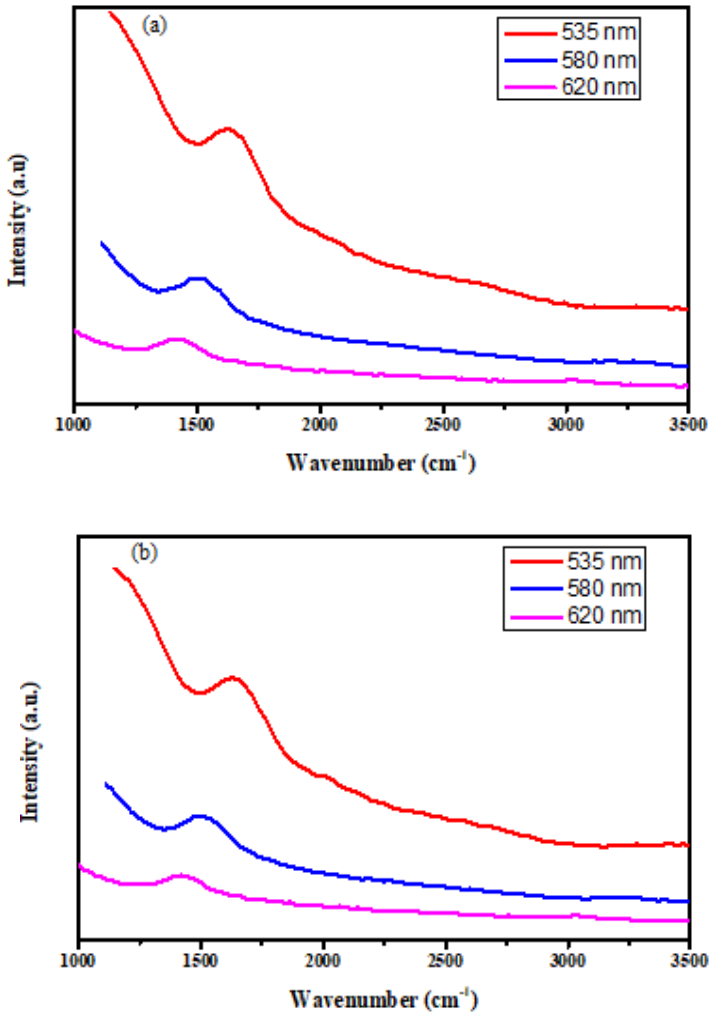

Figure 3.14: Calculated Raman spectrum from emission data of NPs sample: (a) CFO_CN (1) and (b) CFO_CN (2)

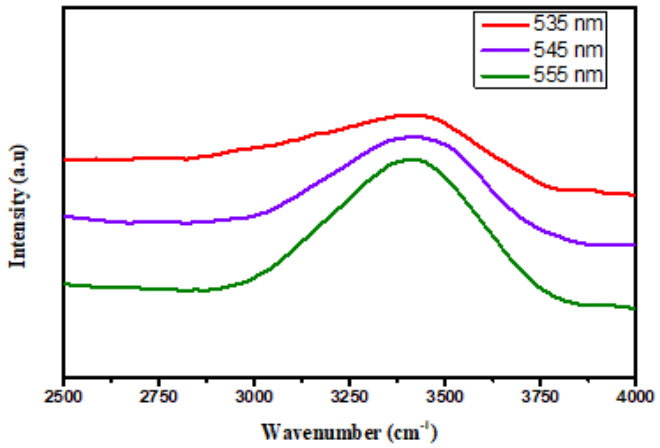

Figure 3.15: Raman shift observation of deionized water for different excitation energy

Finally to find the functional groups and also traces of fluorescence a comparison among carbon-coated CSNPs, CFO_CN (1), and CFO_CN (2) emission spectra were done at a fixed excitation wavelength of 535 nm. (Figure 3.16) Clearly, after introducing DMF in the solution few peaks have appeared due to the interaction of carbon, nitrogen, hydrogen, and CFO NPs. The peaks at 584 and 649 nm are coming from carbon and DI water respectively. Another peak has around 800 nm has started to form, where the wavelength is 1.5 times the excitation

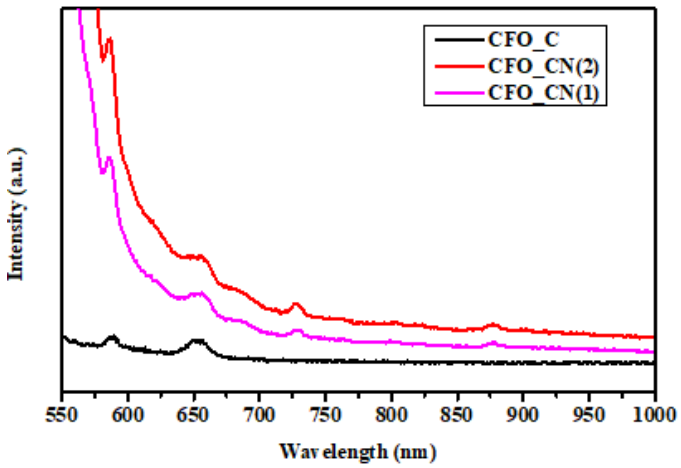

Figure 3.16: Fluorescence plot for NPs sample at 535 nm excitation wavelength

wavelength. This is an artifact that becomes more prominent for higher wavelength excitation. The two other peaks around 730 and 880 nm are coming from some functional groups which are not available in only carbon-coated CSNPs sample. These peaks might be coming from functional groups other than graphitic and CFO structure. To investigate the changes in these two peaks emission spectra was taken from CFO_CN (2) samples as the count for this sample was higher than CFO_CN (1). Figure 3.17 below is showing the emission spectra for different excitation wavelengths from 500-555 nm wavelength range. As it was mentioned earlier that a peak around 1.5 times the excitation wavelength appears for higher wavelength excitation, now this is evident in Figure 3.17 below. For 500 nm excitation that peak is absent and has started to form after 532 nm. For 545 and 555 nm, the count of this peak increased and positioned exactly at 1.5 times the excitation wavelength. The peaks located between 700-775 nm and 850-950 nm

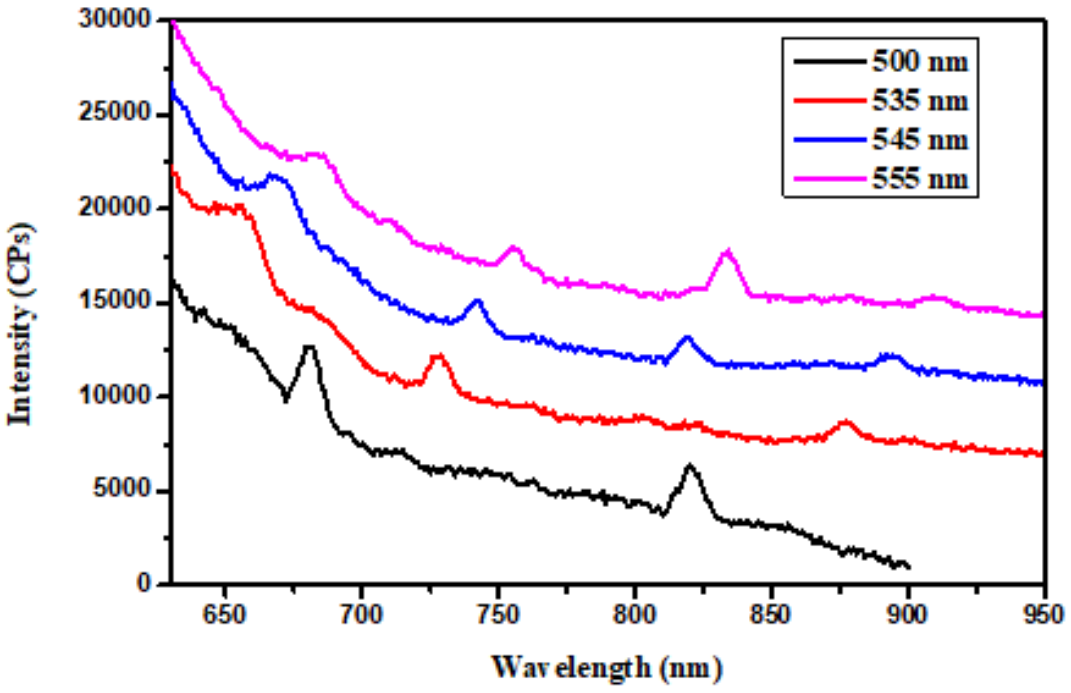

Figure 3.17: Fluorescence spectra of CFO_CN (2) sample at different excitation wavelengths

ranges are changing their position with the excitation wavelength and also decreases in intensity. Thus, they are surely Raman peaks forming in the 3500-4500 wavenumber regions. As individual carbon structure has no Raman peak beyond 3200 cm^{-1}, these peaks might be coming from some other functional groups, further study is needed to determine where they are coming from. Also, to find any fluorescence peak, a higher excitation wavelength can be checked. For possibilities, amine, carboxyl, and cyanide groups could be taken into consideration.

SEM Analysis. Scanning electron microscopy uses reflected or knocked-off electrons from a sample to generate high-resolution imaging with greater magnification. While TEM provides features of the inner structure of a sample, SEM reveals mostly the topography and composition of the sample's surface. The electron beam in SEM can be focused to a fine point of a sample and scan line by a line following a rectangular raster pattern. In conjunction with SEM, there is another technique called energy dispersive spectroscopy (EDS) that does elemental analysis by detecting the characteristic X-rays, emit when the beam electrons collide with an inner shell electron of the sample and scatter it from its position. The EDS elemental quantification can be done at a point or along a line of the sample or can be mapped over a particular area of the sample.

In this work, SEM/EDS spectroscopy of the NPs samples was performed in FEI FESEM Quanta-200F integrated with an enhanced EDS detector facility. All the elemental mappings were done with incident electrons of 10 kV energy and a scanning time of 20 minutes. SEM mapping, Figure 3.18 and Figure 3.19 sorted out interesting structural differences between CFO_C and CFO_CN NPs samples. The core atoms Fe, Co, and O are present highly in both the samples. The intensity count for O is the highest which is followed by Fe, Co and C. As the

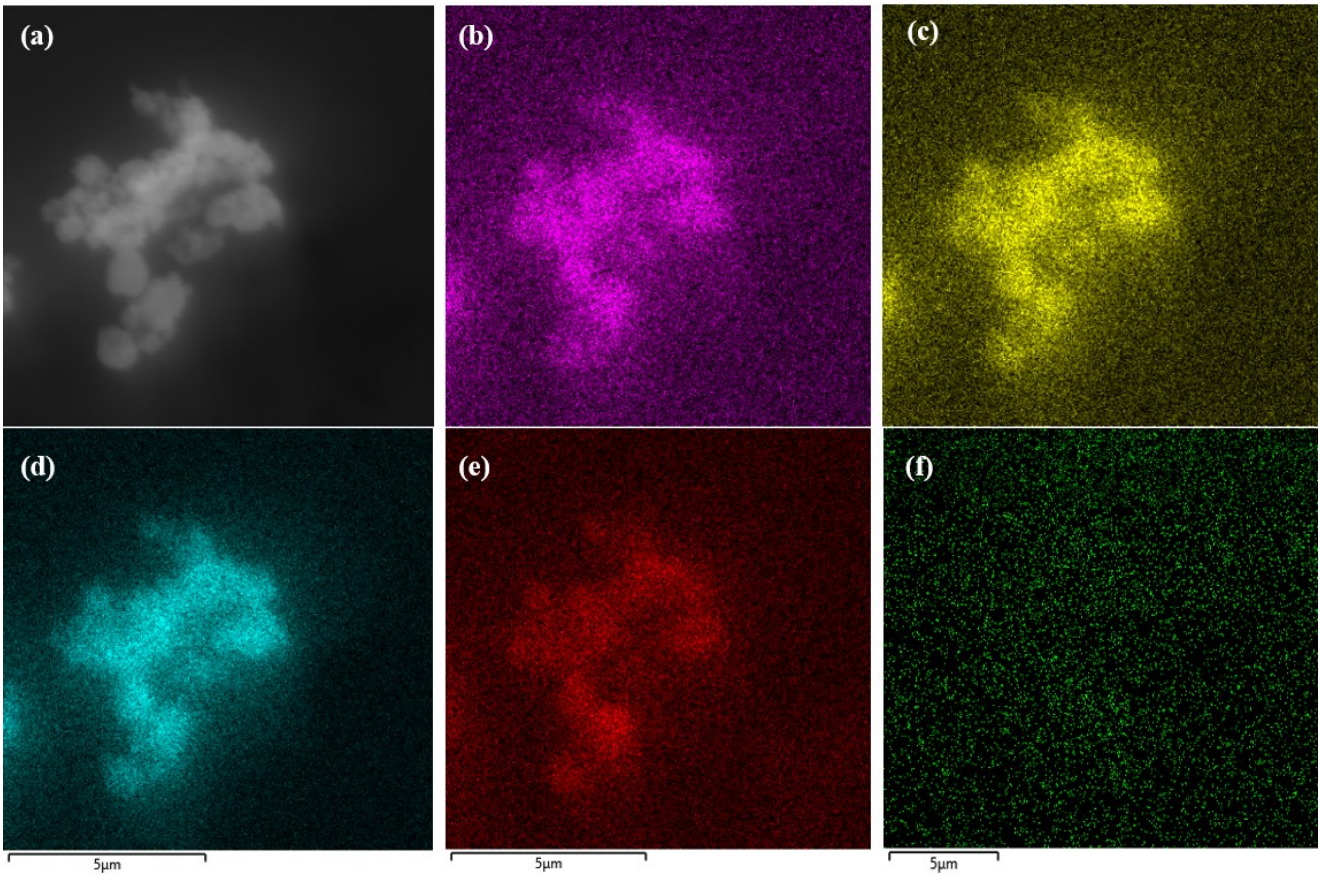

Figure 3.18: SEM images and elemental mapping of CFO_C NPs: (a) SEM of CSNPs, (b) Co atom, (c) Fe atom, (d) O atom, (e) C atom and (f) N atom.

amount of C has mostly presented in the shell region the count is comparatively lower for both the samples. From Figure 3.18, it is observed that the CFO_C sample which was synthesized by ablating a solution of toluene solvent and CFO NPs only, shows no sign of nitrogen present in the NPs. There are little amount of nitrogen counts coming basically from artifacts and distributed equally everywhere in the mapping. As it is not following the NPs, it confirms the absence of nitrogen in the CFO_C sample. On the other hand, the CFO_CN (2) sample displaying a reasonable amount of nitrogen located particularly wherever the NPs are visible in the SEM image. The relative intensity count for the core atoms is similar to before and the C and N counts have increased substantially. The reason behind is compositional changes by the

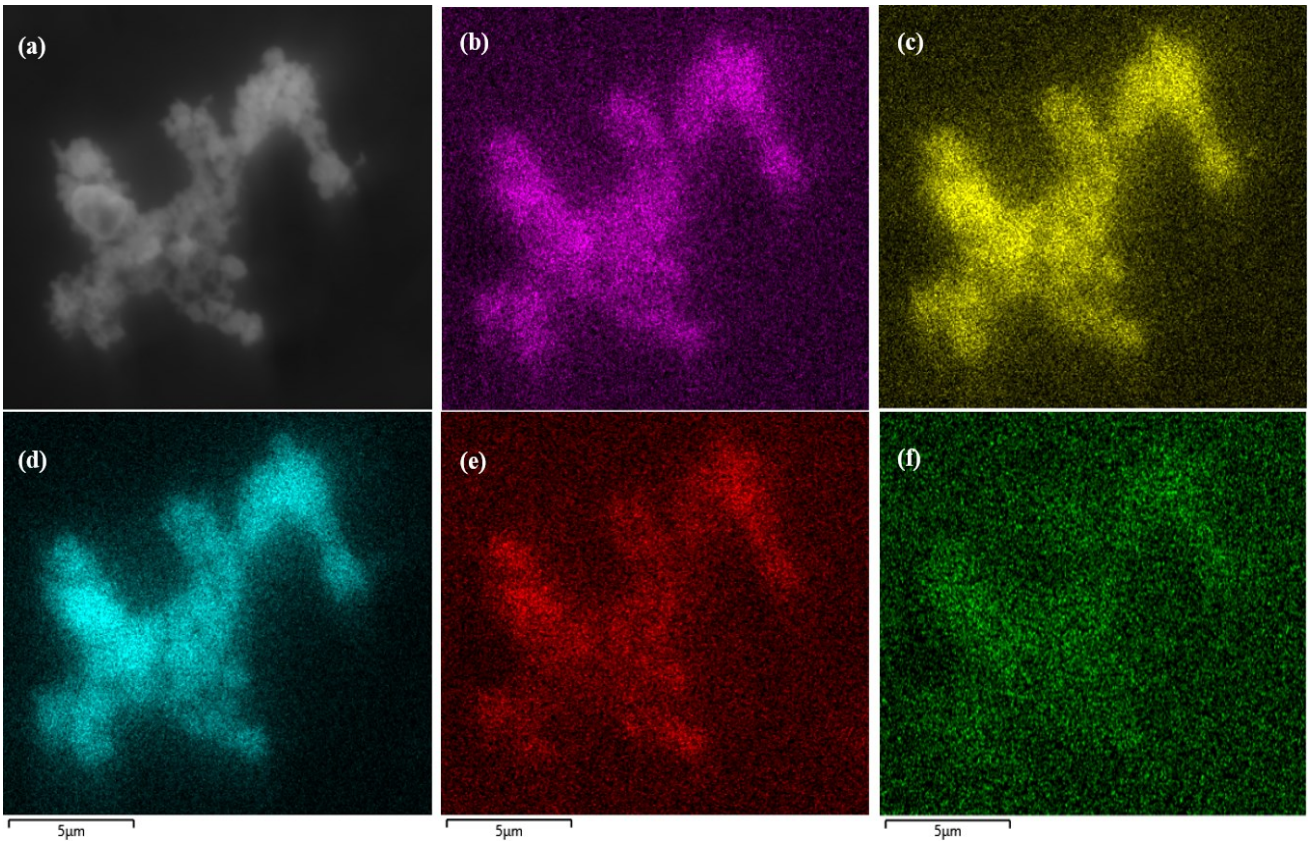

Figure 3.19: SEM images and elemental mapping of CFO_CN NPs: (a) SEM of CSNPs, (b) Co atom, (c) Fe atom, (d) O atom, (e) C atom and (f) N atom.

addition of N, N- DMF is evident in both Figure 3.18 and Figure 3.19 the presence of N, N-DMF in the reaction media along with toluene and CFO NPs. Due to DMF, more number C atoms are available in the solution and that solvent also supplies N after breaking the N-C and N-H bonds. As a result, nitrogen is getting into the shell structure mostly and very few of them might be getting into the voids of CFO crystal structure. Although it is not confirmed the presence of N particularly in the shell structure, mapping data suggests incorporation of N atom through DMF solution is achievable for magnetic CFO CSNPs.

CONCLUSIONS

Carbon coated CFO CSNPs have been synthesized by a controlled method with the application of pulsed laser deposition. The samples made with varying laser shots were characterized by different techniques. The powder x-ray diffraction study revealed the structural phase present in the CFO spinel ferrite nanoparticles and how it is. Raman spectroscopy confirmed the presence of tetrahedral and octahedral sites in CFO nanoparticles and how different modes related to those sites are changing. Besides, the presence of carbon and improved crystallinity with increasing laser ablation has been identified from the Raman spectroscopy. The transmission electron microscopic analysis has shown the structure mapping and uniform shell structure around the core material. Later on, nitrogen incorporation in the synthesis media has inferred detectable changes which are the key factor in synthesizing the multifunctional CSNPs for potential biomedical applications. The elemental mapping from scanning electron microscopic studies detects the presence of nitrogen in the NPs. In the future, electron microscopy studies can be done to determine the nitrogen, specifically in the shell region, and fluorescence analysis to find the particular wavelength region where they can be used for light sensing applications.

REFERENCES

(1) Abdullaeva, Z.; Omurzak, E.; Iwamoto, C.; Ganapathy, H. S.; Sulaimankulova, S.; Liliang, C.; Mashimo, T., Onion-like carbon-encapsulated Co, Ni, and Fe magnetic nanoparticles with low cytotoxicity synthesized by a pulsed plasma in a liquid. *Carbon* **2012,** *50* (5), 1776-1785.

(2) Anderson, S. D.; Gwenin, V. V.; Gwenin, C. D., Magnetic functionalized nanoparticles for biomedical, drug delivery and imaging applications. *Nanoscale research letters* **2019,** *14* (1), 1-16.

(3) Chatterjee, K.; Sarkar, S.; Rao, K. J.; Paria, S., Core/shell nanoparticles in biomedical applications. *Advances in colloid and interface science* **2014,** *209*, 8-39.

(4) Park, J.; Jeong, S.; Jeong, M.; Kim, J.; Cho, B., Synthesis of carbon-encapsulated magnetic nanoparticles by pulsed laser irradiation of solution. *Carbon* **2008,** *46* (11), 1369-1377.

(5) Mirza, A. Z.; Siddiqui, F. A., Nanomedicine and drug delivery: a mini review. *International Nano Letters* **2014,** *4* (1), 94.

(6) Mura, S.; Nicolas, J.; Couvreur, P., Stimuli-responsive nanocarriers for drug delivery. *Nature materials* **2013,** *12* (11), 991-1003.

(7) Rosenblum, D.; Joshi, N.; Tao, W.; Karp, J. M.; Peer, D., Progress and challenges towards targeted delivery of cancer therapeutics. *Nature communications* **2018,** *9* (1), 1-12.

(8) Markides, H.; Rotherham, M.; El Haj, A., Biocompatibility and toxicity of magnetic nanoparticles in regenerative medicine. *Journal of Nanomaterials* **2012,** *2012*.

(9) Jeong, U.; Teng, X.; Wang, Y.; Yang, H.; Xia, Y., Superparamagnetic colloids: controlled synthesis and niche applications. *Advanced Materials* **2007,** *19* (1), 33-60.

(10) Wozniak, M. J.; Wozniak, P.; Bystrzejewski, M.; Cudzilo, S.; Huczko, A.; Jelen, P.; Kaszuwara, W.; Kozubowski, J. A.; Lange, H.; Leonowicz, M., Magnetic nanoparticles of Fe and Nd–Fe–B alloy encapsulated in carbon shells for drug delivery systems: Study of the structure and interaction with the living cells. *Journal of alloys and compounds* **2006,** *423* (1-2), 87-91.

(11) Xu, X.; Gao, L.; Duan, G., The fabrication of Au@ C core/shell nanoparticles by laser ablation in solutions and their enhancements to a gas sensor. *Micromachines* **2018,** *9* (6), 278.

(12) Kim, S.; Shibata, E.; Sergiienko, R.; Nakamura, T., Purification and separation of carbon nanocapsules as a magnetic carrier for drug delivery systems. *Carbon* **2008,** *46* (12), 1523-1529.

(13) Zhao, W.; Gu, J.; Zhang, L.; Chen, H.; Shi, J., Fabrication of uniform magnetic nanocomposite spheres with a magnetic core/mesoporous silica shell structure. *Journal of the American Chemical Society* **2005,** *127* (25), 8916-8917.
(14) Valix, M.; Cheung, W.; Zhang, K., Role of heteroatoms in activated carbon for removal of hexavalent chromium from wastewaters. *Journal of hazardous materials* **2006,** *135* (1-3), 395-405.

(15) Feng, Z.; Li, Z.; Zhang, X.; Shi, Y.; Zhou, N., Nitrogen-doped carbon quantum dots as fluorescent probes for sensitive and selective detection of nitrite. *Molecules* **2017,** *22* (12), 2061.

(16) Treeweranuwat, P.; Boonyoung, P.; Chareonpanich, M.; Nueangnoraj, K., Role of Nitrogen on the Porosity, Surface, and Electrochemical Characteristics of Activated Carbon. *ACS omega* **2020,** *5* (4), 1911-1918.

(17) Kwong, H.; Wong, M.; Leung, C.; Wong, Y.; Wong, K., Formation of core/shell structured cobalt/carbon nanoparticles by pulsed laser ablation in toluene. *Journal of applied physics* **2010,** *108* (3), 034304.

(18) Ding, S.; Jiao, N., Direct Transformation of N, N-Dimethylformamide to− CN: Pd-Catalyzed Cyanation of Heteroarenes via C–H Functionalization. *Journal of the American Chemical Society* **2011,** *133* (32), 12374-12377.

(19) Lee, S.; Jung, H. J.; Choi, H. C.; Hwang, Y. S.; Choi, M. Y., Solvent Acting as a Precursor: Synthesis of AgCN From AgNO3 in N, N-DMF Solvent by Laser Ablation. *Bulletin of the Korean Chemical Society* **2017,** *38* (1), 136-139.

(20) Knaanie, R.; Šebek, J. í.; Tsuge, M.; Myllys, N.; Khriachtchev, L.; Räsänen, M.; Albee, B.; Potma, E. O.; Gerber, R. B., Infrared spectrum of toluene: Comparison of anharmonic isolated-molecule calculations and experiments in liquid phase and in a Ne matrix. *The Journal of Physical Chemistry A* **2016,** *120* (19), 3380-3389.

(21) Davico, G. E.; Bierbaum, V. M.; DePuy, C. H.; Ellison, G. B.; Squires, R. R., The CH bond energy of benzene. *Journal of the American Chemical Society* **1995,** *117* (9), 2590-2599.

(22) Caltun, O.; Chiriac, H.; Lupu, N.; Dumitru, I.; Rao, B. P., High magnetostrictive doped cobalt ferrite. *Journal of Optoelectronics and Advanced Materials* **2007,** *9* (4), 1158.

(23) Melikhov, Y.; Snyder, J. E.; Jiles, D. C.; Ring, A.; Paulsen, J.; Lo, C. C.; Dennis, K. W., Temperature dependence of magnetic anisotropy in Mn-substituted cobalt ferrite. *Journal of Applied Physics* **2006,** *99* (8), 08R102.

(24) Silambarasan, M.; Saravanan, S.; Soga, T., Effect of Fe-doping on the structural, morphological and optical properties of ZnO nanoparticles synthesized by solution combustion process. *Physica E: Low-dimensional Systems and Nanostructures* **2015,** *71*, 109-116.

(25) Chandramohan, P.; Srinivasan, M.; Velmurugan, S.; Narasimhan, S., Cation distribution and particle size effect on Raman spectrum of CoFe2O4. *Journal of Solid State Chemistry* **2011,** *184* (1), 89-96.

(26) Capano, M.; McDevitt, N.; Singh, R.; Qian, F., Characterization of amorphous carbon thin films. *Journal of Vacuum Science & Technology A: Vacuum, Surfaces, and Films* **1996,** *14* (2), 431-435.